Impact of Microwave and mmWave Channel Models on 5G Systems Performance

Callum T. Neil, *Member, IEEE*, Mansoor Shafi, *Life Fellow, IEEE*, Peter J. Smith, *Fellow, IEEE*,
Pawel A. Dmochowski, *Senior Member, IEEE*, and Jianhua Zhang, *Senior Member, IEEE*

Abstract—Channel models and measurements across a wide range of candidate bands for 5G wireless networks are considered. Motivated by the different propagation and spatial characteristics between different bands and channel models within a band, we investigate how key channel modelling and spatial parameter differences impact various antenna topologies in terms of sum rate, channel eigenvalue structure, effective degrees of freedom (EDOF), channel connectivity and massive MIMO convergence. We show that due to the sparsity of millimeter-wave (mmWave) channels, any variation in spatial parameters can dramatically affect the sum rate. In microwave scenarios, where the probability of line-of-sight (LOS) propagation is low, the structure of the eigenvalues is highly dependent on the richness of scattering. In mmWave bands, where the probability of LOS is higher, the structure of the eigenvalues is largely dependent on the LOS channel model. The uniform linear array is seen to have superior sum rate and eigenvalue structure due to the inherently larger inter-element spacings and wider azimuth spectra. These observations are seen to affect sum rate, EDOF and massive MIMO convergence. Two variations of channel connectivity are then considered, and compared with EDOF, to examine the richness of scattering and channel rank.

Index Terms—5G, millimeter-wave (mmWave), channel models, massive multiple-input-multiple-output (MIMO).

I. Introduction

A combination of an unprecedented growth in mobile data traffic [1] and a congested sub-6 GHz spectrum is motivating the research and development of wireless transmission at higher frequencies where large amounts of vacant spectrum lies under-utilized [2], [3]. Specifically, the range of candidate bands being considered for Fifth Generation (5G) wireless systems has recently been extended to include 6-100 GHz [4]. With a combination of massive multiple-input-multiple-output (MIMO) antenna arrays [5] and smaller cell sizes, millimeter-wave (mmWave) technology is expected to be a key enabler in achieving the huge data rates required to meet 5G specifications [1], [6]. 5G is also likely to be introduced for wide area coverage in existing microwave bands. However, frequencies over these bands exhibit enormous variation in channel characteristics. For example, microwave bands provide excellent coverage capabilities but bandwidth is scarce. Whereas mmWave bands have an abundance of available spectrum but suffer from high electromagnetic attenuation [7]. There is, therefore, a need to understand how the differences in

propagation characteristics, such as multipath spreads, over the different frequency bands affects various performance metrics. Motivated by this, channel models over a wide range of frequency bands are considered.

Microwave bands have a standardized three-dimensional (3D) spatial channel model (SCM), developed by the 3rd Generation Partnership Project (3GPP) [8], for frequencies below 6 GHz. Here, a non-line-of-sight (NLOS), i.e. scattered, channel path is modelled following the Saleh-Valenzuela (S-V) [9] SCM, while line-of-sight (LOS) propagation is modelled via a Rician channel [10] extension of the NLOS component. On the other hand, standardized SCMs for intermediate (6-30 GHz) and mmWave (30-100 GHz) frequency bands are in their early stages of development, with just a single published standard for frequencies above 6 GHz [11]. As in [11] and the majority of standardized SCMs below 6 GHz, it is likely that mmWave SCMs will follow a S-V-like structure. As a result, there have been many recent mmWave measurement campaigns which replicate the structure in [8] and [11], or minor variations thereof. For example, the SCM presented by Akdeniz et al., in [12], for 28 and 73 GHz follows a path loss (PL) scaled S-V structure. This type of SCM is used widely in analysing beamforming techniques at mmWave frequencies, for example [13], [14]. Thus, frequency bands can not only be differentiated by slight variations in SCMs, but also by differences in key spatial parameters which form the basis of the complex channel impulse response. A detailed discussion of the differences in the SCMs considered is left to Sec. II-C.

In this paper, we include a measurement campaign at 6 GHz, consider standardized SCMs [8], proposed SCMs [15] and recently published measurement campaigns [12], [16]–[19], across a variety candidate frequency bands. We also consider the recent standardized 3GPP SCM for frequencies above 6 GHz [11]. We identify key SCM parameter differences between different frequency bands and different SCMs in the same frequency band. In turn, we investigate how these key parameters impact sum rate, eigenvalue distributions and convergence to massive MIMO properties. Note that while some similar results were presented in [20], in this paper a much larger range of microwave and mmWave band SCMs are considered, including new measurements, in much more detail. Furthermore, the results of [20] are extended to include a study on cross-polarized (x-pol) antennas, directive antenna patterns (APs) and a channel connectivity measure [21], [22].

The contributions of this paper are as follows:

1) We examine the impact of intra-cluster angular spreads, x-pol antennas, directive APs and user numbers for different antenna topologies on the sum rates of different SCMs across microwave and mmWave bands.

C.T. Neil and P.A. Dmochowski are with the School of Engineering and Computer Science, Victoria University of Wellington, Wellington, New Zealand (e-mail: {callum.neil,pawel.dmochowski}@vuw.ac.nz).

M. Shafi is with Spark NZ, Wellington 6011, New Zealand (e-mail: mansoor.shafi@spark.co.nz).

P.J. Smith is with the School of Mathematics and Statistics, Victoria University of Wellington, Wellington, New Zealand (e-mail: peter.smith@vuw.ac.nz).

J. Zhang is with the State Key Lab of Networking and Switching Technology, Beijing University of Posts and Telecommunications, Beijing, China (e-mail: jhzhang@bupt.edu.cn).

2) We investigate the impacts of inter-element antenna spacings, receiver antenna numbers, propagation type and user numbers on the eigenvalue structures of various antenna topologies for different SCMs across microwave and mmWave bands.

3) We extend the effective degrees of freedom (EDOF) definition in [23] to measure the total number of data streams a multi-user system can support. We then show how EDOF is affected by different antenna topologies, SCMs, numbers of users and receive antennas.

4) We consider two variations of the channel connectivity measure in [21], [22] to examine the richness of scattering and channel rank over different frequency bands, and subsequently compare this to the EDOF measure.

5) We explore the convergence to massive MIMO by considering the eigenvalue ratio. We show that the rate of convergence is dependent on the environment, antenna topology and user separation.

This paper is organized as follows. The SCMs considered, as well as key channel modelling differences among them, are explained in Sec. II. In Sec. III, the antenna array topologies and simulation details are discussed. In Sec. IV, V, VI, VII and VIII we investigate the effects of key system and channel modelling parameters on the resultant system sum rate, eigenvalue properties, EDOF, channel connectivity and convergence to favourable propagation, respectively. In Sec. IX we conclude the paper.

II. CHANNEL MODELS

In this section we detail the cellular environments considered, along with their respective SCM structure. We also provide a detailed discussion of the key modelling differences between the environments.

We consider the following cellular environments:

1) *3GPP 2.6 GHz*: The standardized SCM, for frequencies below 6 GHz, detailed in [8].

2) *BUPT 6 GHz*: Outdoor 6 GHz measurements following the 3GPP SCM, with a detailed measurement methodology given in [24].

3) *Akdeniz 28 GHz*: New York University (NYU) 28 GHz measurements, given in [12].

4) *Hur 28 GHz*: 28 GHz measurements from a Samsung Electronics, University of Southern California (USC), NYU, and Aalto University collaboration [17].

5) *Samimi 28 GHz*: NYU 28 GHz measurements [18].

6) *WPC 28 GHz*: White paper collaboration (WPC) 28 GHz measurements, given in [16].

7) *Thomas 73 GHz*: 73 GHz measurements from a Nokia, Aalborg University, and NYU collaboration [19].

8) *Samimi 73 GHz*: NYU 73 GHz measurements [18].

9) *WPC 73 GHz*: WPC 73 GHz measurements [16].

Note that the Samimi 28 and 73 GHz measurements in [18] are for the SCM presented in [15], which extends a two-dimensional (2D) ultra-wideband mmWave SCM given in [25][1]. The corresponding omnidirectional PL measurements

[1]Note: we consider a narrowband SCM and therefore ignore the time and angular space correlation (lobe) extension described in [25].

are given in [26]. All simulation environments, *including BUPT measurements*, use either variations of the 3GPP SCM or the Akdeniz SCM. For conciseness, we present the two SCMs and then discuss the 3GPP SCM variations and subtle environmental differences in Sec. II-C. For space reasons, we omit the detailed steps required to generate the parameters of the two SCMs, but refer the reader to [8] and [12]. However, we do present the key simulation steps in Sec. III-B.

We consider a single-cell downlink (DL) system where an M antenna element BS serves K users, each with N antenna elements, in one time/frequency resource. The composite DL channel matrix from the BS to all user's is given by $\mathbf{H} = \left[\mathbf{H}_1^{\mathrm{T}}, \ldots, \mathbf{H}_K^{\mathrm{T}} \right]^{\mathrm{T}}$, where $\mathbf{H}_k$ denotes the kth users $N \times M$ channel matrix. It is assumed that there is no mobility amongst users (or the BS).

A. 3GPP SCM [8]

As standardized by 3GPP [8], for frequencies below 6 GHz, the kth user's $N \times M$ channel matrix can be described as

$$
\begin{aligned}
\mathbf{H}_k = &\frac{1}{\sqrt{10^{0.1P}}} \left(\sqrt{\frac{1}{1+\kappa}} \sum_{c=1}^{C} \sqrt{\frac{\gamma_c}{L}} \sum_{l=1}^{L} \begin{bmatrix} F_{\mathrm{RX}}^\theta \left(\phi_{c,l}^{\mathrm{AOA}}, \theta_{c,l}^{\mathrm{AOA}} \right) \\ F_{\mathrm{RX}}^\phi \left(\phi_{c,l}^{\mathrm{AOA}}, \theta_{c,l}^{\mathrm{AOA}} \right) \end{bmatrix}^{\mathrm{T}} \right. \\
&\times \begin{bmatrix} \exp\left(j\psi_{c,l}^{\theta,\theta} \right) & \sqrt{\varkappa_{c,l}^{-1}} \exp\left(j\psi_{c,l}^{\theta,\phi} \right) \\ \sqrt{\varkappa_{c,l}^{-1}} \exp\left(j\psi_{c,l}^{\phi,\theta} \right) & \exp\left(j\psi_{c,l}^{\phi,\phi} \right) \end{bmatrix} \\
&\times \begin{bmatrix} F_{\mathrm{TX}}^\theta \left(\phi_{c,l}^{\mathrm{AOD}}, \theta_{c,l}^{\mathrm{AOD}} \right) \\ F_{\mathrm{TX}}^\phi \left(\phi_{c,l}^{\mathrm{AOD}}, \theta_{c,l}^{\mathrm{AOD}} \right) \end{bmatrix} \mathbf{a}_{\mathrm{RX}} \left(\phi_{c,l}^{\mathrm{AOA}}, \theta_{c,l}^{\mathrm{AOA}} \right) \mathbf{a}_{\mathrm{TX}}^{\mathrm{H}} \left(\phi_{c,l}^{\mathrm{AOD}}, \theta_{c,l}^{\mathrm{AOD}} \right) \\
&+ \sqrt{\frac{\kappa}{1+\kappa}} \begin{bmatrix} F_{\mathrm{RX}}^\theta \left(\varphi^{\mathrm{AOA}}, \vartheta^{\mathrm{AOA}} \right) \\ F_{\mathrm{RX}}^\phi \left(\varphi^{\mathrm{AOA}}, \vartheta^{\mathrm{AOA}} \right) \end{bmatrix}^{\mathrm{T}} \begin{bmatrix} \exp\left(j\Psi \right) & 0 \\ 0 & -\exp\left(j\Psi \right) \end{bmatrix} \times \\
&\left. \begin{bmatrix} F_{\mathrm{TX}}^\theta \left(\varphi^{\mathrm{AOD}}, \vartheta^{\mathrm{AOD}} \right) \\ F_{\mathrm{TX}}^\phi \left(\varphi^{\mathrm{AOD}}, \vartheta^{\mathrm{AOD}} \right) \end{bmatrix} \mathbf{a}_{\mathrm{RX}} \left(\varphi^{\mathrm{AOA}}, \vartheta^{\mathrm{AOA}} \right) \mathbf{a}_{\mathrm{TX}}^{\mathrm{H}} \left(\varphi^{\mathrm{AOD}}, \vartheta^{\mathrm{AOD}} \right) \right),
\end{aligned}
\tag{1}
$$

where P is the PL, κ is the Rician K-factor, C is the number of clusters, γ_c is the normalized power of cluster $c \in 1, \ldots, C$, L is the number of subpaths per-cluster and $\varkappa_{c,l}$ is the cross-polarization power ratio (XPR) of subpath $l \in 1, \ldots, L$ in cluster c. The angles $\phi_{c,l}^{\mathrm{AOA}} \in [0, 2\pi)$, $\theta_{c,l}^{\mathrm{AOA}} \in [0, \pi)$, $\phi_{c,l}^{\mathrm{AOD}} \in [0, 2\pi)$ and $\theta_{c,l}^{\mathrm{AOD}} \in [0, \pi)$ denote the azimuth angle of arrival (AOA), elevation AOA, azimuth AOD and elevation AOD, respectively, of subpath l in cluster c. Note that the coordinate system is chosen such that the antenna array broadside is at $\phi = \pi/2$ and $3\pi/2$ for azimuth angles and $\theta = \pi/2$ for elevation angles. Also, $\varphi^{\mathrm{AOA}} \in [0, 2\pi)$, $\vartheta^{\mathrm{AOA}} \in [0, \pi)$, $\varphi^{\mathrm{AOD}} \in [0, 2\pi)$ and $\vartheta^{\mathrm{AOD}} \in [0, \pi)$ denote the azimuth AOA, elevation AOA, azimuth AOD and elevation AOD, respectively, of the LOS angle between the BS and user. $\psi_{c,l}^{\theta,\theta} \sim \mathcal{U}[0, 2\pi)$, $\psi_{c,l}^{\theta,\phi} \sim \mathcal{U}[0, 2\pi)$, $\psi_{c,l}^{\phi,\theta} \sim \mathcal{U}[0, 2\pi)$ and $\psi_{c,l}^{\phi,\phi} \sim \mathcal{U}[0, 2\pi)$ denote the random initial phases of the four different polarization combinations $\{(\theta, \theta); (\theta, \phi); (\phi, \theta); (\phi, \phi)\}$ of subpath l in cluster c. Likewise, $\Psi \sim \mathcal{U}[0, 2\pi)$ is the random initial phase of the LOS path. $\mathbf{a}_{\mathrm{RX}}(\phi_{c,l}^{\mathrm{AOA}}, \theta_{c,l}^{\mathrm{AOA}})$ and $\mathbf{a}_{\mathrm{TX}}(\phi_{c,l}^{\mathrm{AOD}}, \theta_{c,l}^{\mathrm{AOD}})$ denote the $N \times 1$ RX and $M \times 1$ TX NLOS antenna array

response vectors, respectively, given by

$$\mathbf{a}_{\text{RX}}\left(\phi_{c,l}^{\text{AOA}}, \theta_{c,l}^{\text{AOA}}\right) = \exp\left(j\frac{2\pi}{\lambda}\mathbf{W}_{\text{RX}}\mathbf{r}\left(\phi_{c,l}^{\text{AOA}}, \theta_{c,l}^{\text{AOA}}\right)\right), \quad (2)$$

$$\mathbf{a}_{\text{TX}}\left(\phi_{c,l}^{\text{AOD}}, \theta_{c,l}^{\text{AOD}}\right) = \exp\left(j\frac{2\pi}{\lambda}\mathbf{W}_{\text{TX}}\mathbf{r}\left(\phi_{c,l}^{\text{AOD}}, \theta_{c,l}^{\text{AOD}}\right)\right), \quad (3)$$

where $\mathbf{W}_{\text{RX}}$ and $\mathbf{W}_{\text{TX}}$ are the $N \times 3$ and $M \times 3$ location matrices of the RX and TX antenna elements in 3D Cartesian coordinates, respectively. $\mathbf{r}(\phi_{c,l}^{\text{AOA}}, \theta_{c,l}^{\text{AOA}})$ and $\mathbf{r}(\phi_{c,l}^{\text{AOD}}, \theta_{c,l}^{\text{AOD}})$ denote the 3×1 spherical unit vectors of the NLOS AOAs and NLOS AODs, respectively, where $\mathbf{r}(\phi, \theta) = [\sin(\theta)\cos(\phi), \sin(\theta)\sin(\phi), \cos(\theta)]^{\text{T}}$. The LOS antenna array response vectors, $\mathbf{a}_{\text{RX}}(\varphi^{\text{AOA}}, \vartheta^{\text{AOA}})$ and $\mathbf{a}_{\text{TX}}(\varphi^{\text{AOD}}, \vartheta^{\text{AOD}})$ are generated the same way as the NLOS antenna array response vectors. $\{F_{\text{RX}}^\theta, F_{\text{RX}}^\phi\}$ and $\{F_{\text{TX}}^\theta, F_{\text{TX}}^\phi\}$ denote the vertically and horizontally polarized AP pairs of the RX and TX, respectively. Rewriting (1) as $\mathbf{H}_k = \sqrt{10^{-0.1P}}\widetilde{\mathbf{H}}_k$, we note that the large scale fading is captured by $\sqrt{10^{-0.1P}}$ while the fast fading and LOS components are in $\widetilde{\mathbf{H}}_k$. The matrix $\widetilde{\mathbf{H}}_k$ is not perfectly normalized as the power of each element depends on the APs and the XPR.

Since vertically polarized (v-pol) antenna elements with omnidirectional APs are used in many of the measurement campaigns considered, we will assume this layout for most of the paper for a fair comparison between each environment, i.e., $F_{\text{TX}}^\theta = F_{\text{RX}}^\theta = 1$ and $F_{\text{TX}}^\phi = F_{\text{RX}}^\phi = 0$. However, in Sec. IV-B, we also provide a small study of the effects of x-pol antenna elements, with and without directive APs at the TX, for the 3GPP 28 GHz environment [11], which standardizes both x-pol and directive AP modelling approaches. The definition of the APs with x-pol antennas are left to Sec. IV-B.

From (1), the (simplified) 3GPP microwave SCM for v-pol antenna elements with omnidirectional APs is given as

$$\mathbf{H}_k = \frac{1}{\sqrt{10^{0.1P}}}\left(\sqrt{\frac{1}{1+\kappa}}\sum_{c=1}^{C}\sqrt{\frac{\gamma_c}{L}}\sum_{l=1}^{L}\exp\left(j\psi_{c,l}^{\theta,\theta}\right)\right.$$

$$\times \mathbf{a}_{\text{RX}}\left(\phi_{c,l}^{\text{AOA}}, \theta_{c,l}^{\text{AOA}}\right)\mathbf{a}_{\text{TX}}^{\text{H}}\left(\phi_{c,l}^{\text{AOD}}, \theta_{c,l}^{\text{AOD}}\right) + \sqrt{\frac{\kappa}{1+\kappa}}\exp\left(j\Psi\right)$$

$$\left.\times \mathbf{a}_{\text{RX}}\left(\varphi^{\text{AOA}}, \vartheta^{\text{AOA}}\right)\mathbf{a}_{\text{TX}}^{\text{H}}\left(\varphi^{\text{AOD}}, \vartheta^{\text{AOD}}\right)\right). \quad (4)$$

B. Akdeniz SCM [12]

The $N \times M$ channel matrix for the kth user is [12]

$$\mathbf{H}_k = \sum_{c=1}^{C}\frac{1}{\sqrt{L}}\sum_{l=1}^{L}g_{c,l}\mathbf{a}_{\text{RX}}\left(\phi_{c,l}^{\text{AOA}}, \theta_{c,l}^{\text{AOA}}\right)\mathbf{a}_{\text{TX}}^{\text{H}}\left(\phi_{c,l}^{\text{AOD}}, \theta_{c,l}^{\text{AOD}}\right), \quad (5)$$

where $\mathbf{a}_{\text{RX}}(\phi_{c,l}^{\text{AOA}}, \theta_{c,l}^{\text{AOA}})$ and $\mathbf{a}_{\text{TX}}(\phi_{c,l}^{\text{AOD}}, \theta_{c,l}^{\text{AOD}})$ are defined in (2) and (3), respectively, and $g_{c,l} \sim \mathcal{CN}(0, \gamma_c 10^{-0.1P})$ is the independent and identically distributed (i.i.d.) complex small scale fading. All other parameters have the same interpretation as in the 3GPP SCM, in Sec. II-A. The simpler channel models in (4) and (5) are perfectly normalized in that the elements of the fast fading/LOS matrix have unit power scaled by $10^{-0.1P}$ to account for large scale fading. Hence, $\mathbb{E}\left[\text{tr}\left(\mathbf{H}_k\mathbf{H}_k^{\text{H}}\right)\right] = 10^{-0.1P}NM$.
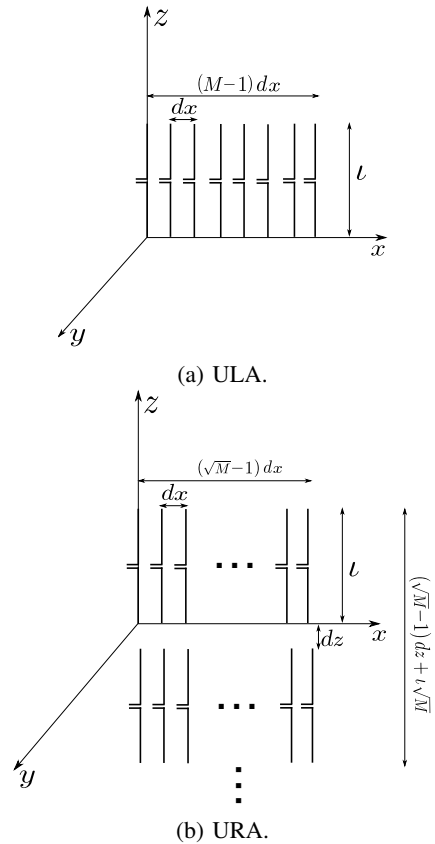

(a) ULA.

(b) URA.

Fig. 1: TX antenna array topologies

C. Key Channel Modelling Differences

3GPP, BUPT, Hur and WPC environments follow the 3GPP SCM, detailed in Sec. II-A, with a different set of parameters used for users in LOS and NLOS propagation. A Rician K-factor is only defined for LOS propagation here. In contrast, Samimi and Thomas environments use the 3GPP SCM, but with slight variations. In the case of the Samimi environment, a (different) Rician K-factor, κ, is defined for both LOS and NLOS users. The Thomas 73 GHz simulation environment differs from 3GPP SCM as it only defines a single set of spatial parameters for all users, regardless of their LOS or NLOS state. In this model, users are solely differentiated by different PL and shadow fading parameters.

On the other hand, the Akdeniz measurements use the SCM described in Sec. II-B, which is a S-V SCM [9]. However, unlike the 3GPP SCM, the Akdeniz SCM does not use a Rician channel [27] to model LOS propagation. Instead, the Akdeniz SCM only modifies the variance of the complex small scale fading coefficient, which is scaled by the (LOS or NLOS) PL from the BS to the user.

The generation of the central cluster angles differs between the 3GPP and Akdeniz SCMs. In the case of the Akdeniz SCM, the azimuth central cluster angles, $\phi_{0,c}^{\text{AOA}}$ and $\phi_{0,c}^{\text{AOD}}$, are generated as uniform random variables over the entire range of azimuth angles, $\phi \in [0, 2\pi)$. Here, also, the elevation central cluster angles, $\theta_{0,c}^{\text{AOA}}$ and $\theta_{0,c}^{\text{AOD}}$, are defined to be the LOS angle between the BS and user, i.e., $\theta_{0,c}^{\text{AOA}} = \vartheta^{\text{AOA}}$ and $\theta_{0,c}^{\text{AOD}} = \vartheta^{\text{AOD}}$. In contrast, for all environments which follow

the basic 3GPP SCM structure, the azimuth and elevation central cluster angles are derived from wrapped Gaussian and Laplacian distributions, respectively, with random root mean squared (RMS) angular spreads.

III. System Description

In this section we detail the antenna topologies considered, give a summary of the simulation steps for one channel realization, describe the key system and environmental specific parameters, and SCM assumptions. We also give a discussion on mmWave beamforming (BF) techniques, which although not considered in this paper, are inherently related to SCMs.

A. Antenna Array Topologies

In this paper, we consider the following two antenna topologies, shown in Fig. 1 for the TX: a ULA along the x-axis and a URA on the x, z-plane. The URA is infact a square array constructd by placing $\sqrt{M}$ ($\sqrt{N}$) rows of $\sqrt{M}$ ($\sqrt{N}$) TX (RX) antennas. Antenna array response vectors for each topology are given in (2) and (3), where $\mathbf{W}_{\mathrm{RX}}$ and $\mathbf{W}_{\mathrm{TX}}$ are antenna topology specific.

B. Simulation Description

A summary of the simulation steps required to generate a *single channel realization* of each users channel, described in (4) and (5), is given below:

1) Calculate location matrices of the TX and RX antenna elements, $\mathbf{W}_{\mathrm{TX}}$ and $\mathbf{W}_{\mathrm{RX}}$ based on the antenna topology and inter-element antenna spacings d_λ.
2) Calculate the noise power from bandwidth, B.
3) Calculate the cell radius, r, from the cell-edge SNR, ρ.
4) For each user:
   a) "Drop" user within a circular coverage region of radius, r, based on area coverage, and randomly generate all LOS angles $\varphi^{\mathrm{AOA}}, \varphi^{\mathrm{AOD}}, \vartheta^{\mathrm{AOA}}, \vartheta^{\mathrm{AOD}}$.
   b) Assign either LOS or NLOS propagation to the user based on the probability of LOS propagation.
   c) For environments which model spatial correlation (SC) between large-scale parameters (3GPP, BUPT, WPC and Hur) calculate shadow fading, ξ, Rician K-factor, κ, and $\phi^{\mathrm{AOA}}, \phi^{\mathrm{AOD}}, \theta^{\mathrm{AOA}}$ and θ^{AOD} inter-cluster spreads.
5) For environments which model SC between large-scale parameters: compute relative distances between each user, and find spatially correlated ξ, κ and $\phi^{\mathrm{AOA}}, \phi^{\mathrm{AOD}}, \theta^{\mathrm{AOA}}, \theta^{\mathrm{AOD}}$ inter-cluster spreads.
6) For each user:
   a) Based on its LOS/NLOS state, obtain shadow fading, ξ, PL, P, Rician K-factor, κ, number of clusters, C, the number of subpaths per cluster, L, and mean intra-cluster angular spreads, $\sigma_\phi^{\mathrm{AOA}}, \sigma_\phi^{\mathrm{AOD}}, \sigma_\theta^{\mathrm{AOA}}, \sigma_\theta^{\mathrm{AOD}}$. Note that there is no Rician K-factor for the Akdeniz SCM.
   b) For each cluster:
      i) Compute cluster power, γ_c.
      ii) Generate azimuth and elevation central cluster angles, $\phi_0^{\mathrm{AOA}}, \phi_0^{\mathrm{AOD}}, \theta_0^{\mathrm{AOA}}, \theta_0^{\mathrm{AOD}}$.

iii) Calculate intra-cluster angular spreads, $\sigma_\phi^{\mathrm{AOA}}, \sigma_\phi^{\mathrm{AOD}}, \sigma_\theta^{\mathrm{AOA}}, \sigma_\theta^{\mathrm{AOD}}$.
iv) For each subpath:
   A) Based on the intra-cluster angular spreads, compute the perturbation (from the central cluster) angles, $\Delta\phi_{c,l}^{\mathrm{AOA}}, \Delta\phi_{c,l}^{\mathrm{AOD}}, \Delta\theta_{c,l}^{\mathrm{AOA}}, \Delta\theta_{c,l}^{\mathrm{AOD}}$, and thus find the angle of each subpath.
   B) Compute NLOS antenna array response vectors, $\mathbf{a}_{\mathrm{RX}}(\phi_{c,l}^{\mathrm{AOA}}, \theta_{c,l}^{\mathrm{AOA}})$ and $\mathbf{a}_{\mathrm{TX}}(\phi_{c,l}^{\mathrm{AOD}}, \theta_{c,l}^{\mathrm{AOD}})$.
   C) For the Akdeniz SCM, compute $g_{c,l}$. For all other channels, compute NLOS vertical polarization, $\exp(j\psi_{c,l}^{\theta,\theta})$ and thus the NLOS channel for each subpath.
   c) Sum over all clusters and subpaths to obtain the NLOS channel.
   d) For all other channels except Akdeniz, with users in LOS propagation:
      i) Compute LOS antenna array response vectors, $\mathbf{a}_{\mathrm{RX}}(\varphi^{\mathrm{AOA}}, \vartheta^{\mathrm{AOA}})$ and $\mathbf{a}_{\mathrm{TX}}(\varphi^{\mathrm{AOD}}, \vartheta^{\mathrm{AOD}})$.
      ii) Compute LOS polarization, $\exp(j\Psi)$ and thus the LOS channel.
      iii) Scale the NLOS and LOS channels via the Rician K-factor and thus compute the composite channel matrix.
   e) Scale the channel matrix via the PL to obtain $\mathbf{H}_k$.

Following the above, the cumulative distribution functions (CDFs) are generated by computing a desired metric, e.g., sum rate CDF, from 5000 channel realizations. Likewise, Monte-Carlo averaging (over all 5000 channel realizations) is used to compute other figures reliant on the channel.

In all simulations the bandwidth is $B = 100$ MHz and cell edge received signal-to-noise-ratio (SNR) is -5 dB. Although mmWave systems typically have higher bandwidth, low TX powers and strong blocking [28] (resulting in a low received SNR), it is assumed that the bandwidth and received SNR is the same over all environments and frequencies considered such that insights into the spatial and statistical differences of the various channels can be drawn. Here, we have assumed that 5G waveforms have an orthogonal frequency-division multiplexing (OFDM) structure, where the resource blocks are made up of narrow band sub-carriers, and therefore can neglect the effects of frequency selectivity. We also assume a noise figure of 8 dB, a fixed TX power of 15 dBm (independent of user numbers and carrier frequency) and a gain per TX antenna element of 10 dBi. The PL to each user is calculated via the close-in (CI) free space reference model [16], [26],

$$P = \alpha + 10\beta \log_{10}(d) + \xi \text{ (dB)}, \qquad (6)$$

where α is the PL constant offset value, β is the PL attenuation constant and $\xi \sim \mathcal{N}(0, \epsilon^2)$ is the PL shadow fading, with variance ϵ^2. Cell radii, r, for each environment are then derived from this based on 90% area coverage [29]. In Fig. 2 we show the dependence of cell radius, r, on the carrier frequency, f, and the number of users, K, for $M = 256$ and a cell edge SNR of -5 dB. It can be seen that as both f and K are

increased, the cell radius, r, is reduced. Firstly, the TX power of 15 dBm is fixed and is thus divided equally between K users. Therefore, when K increases, the cell radius is seen to reduce exponentially to maintain the same average received SNR per user. Secondly, as detailed in Table I, when the carrier frequency increases, the PL constant offset value, α, is also increased due to higher signal attenuation [3].
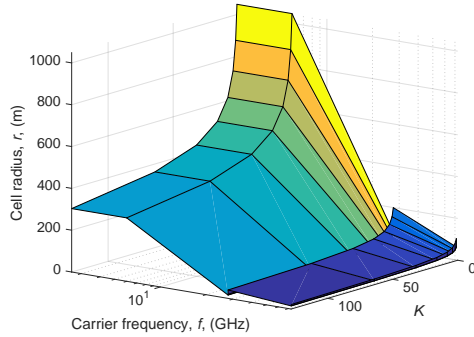

Fig. 2: Cell radius, r, as a function of the number of users, K, and carrier frequency, f, for $M = 256$.

In general, the probability of LOS propagation, p_{LOS}, has been shown to increase with carrier frequency [3], [28], predominantly due to smaller cell-radii (seen in Fig. 2). All p_{LOS} models are thus given as a function of distance for the various SCMs. In Fig. 3, we summarize the probability of LOS, p_{LOS}, as a function of BS to user distance, d, for each environment, which use one of four different p_{LOS} models. The circles represent the cell radii, where $M = 256$ and $K = 8$, based on the link budget parameters described above. Four different LOS probability models can be seen, where for a given distance, the Hur model gives the highest p_{LOS}. The mmWave environments are seen to have smaller cell radii and thus increased LOS probability for a typical user distance compared with the microwave environments.
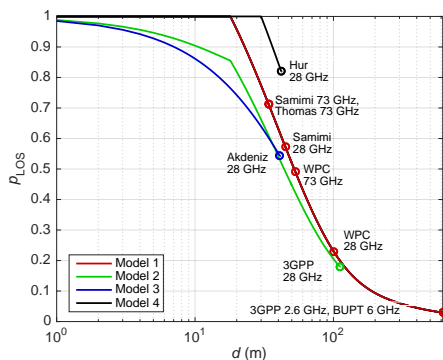

Fig. 3: Probability of LOS propagation, p_{LOS}, as a function of BS to user distance, d, for different simulation environments. See the references [8], [11], [12] and [17] for Model 1,2 3 and 4, respectively.

In the 3GPP, BUPT, Hur and WPC environments, SC between different users' shadow fading parameters, ϵ, Rician K-factors, κ, and inter-cluster RMS angular spreads is defined as a function of a reference distance. Additionally, in the 3GPP 28 GHz environment, SC is defined between different users'

intra-cluster angular spreads, σ, and cluster shadow fading, and XPR. For two users, $k, k' \in 1, \ldots, K$, the SC of a particular parameter, $\rho(d_{k,k'})$, is defined as a function of their distance, $d_{k,k'}$, via [8], [30]

$$\rho(d_{k,k'}) = \exp\left(-d_{k,k'}/d_{\text{SC}}\right), \qquad (7)$$

where d_{SC} denotes the SC reference distance. d_{SC} and all other key environmental statistical spatial parameters are detailed in Table I. Here, ϕ_0 and θ_0 denote the central cluster angles of the azimuth and elevation domains, respectively, σ_ϕ and σ_θ denote the intra-cluster angular spreads of the azimuth and elevation subpaths, respectively. Note that the intra-cluster elevation AOD spread, $\sigma_\theta^{\text{AOD}}$, is not specified for the Akdeniz environment. Here, we therefore assume that $\sigma_\phi^{\text{AOD}}/\sigma_\theta^{\text{AOD}} = \sigma_\phi^{\text{AOA}}/\sigma_\theta^{\text{AOA}}$. Also, the inter-cluster θ^{AOD} RMS spreads are not given for Samimi 28 GHz and 73 GHz channels. We assume that these values are equal to the ones given in the standardized 3GPP 2.6 GHz environment.

C. 5G Beamforming Techniques

Although not considered in this paper, in this section we briefly discuss different (multi-user) BF approaches for mmWave channels. Due to the sparse nature of the mmWave channels (seen by observing the parameters in Table I), and the large number of TX antennas required to overcome link budget issues, effective mmWave BF solutions are expected to leverage the channel sparsity while also being low in complexity, cost and power consumption [31]. Hybrid (analog and digital) BF (HBF) is one way to reduce the BS hardware complexity, cost and power consumption, where the number of radio frequency (RF) chains is much less than the number of TX antennas [14], [32]. Here, there are two different architectures: i) *fully connected* architectures, where all RF chains are connected to all TX antenna elements, and ii) *sub-array* architectures, where each RF chain is connected to a subset of the TX antenna elements. The sub-array architecture can sacrifice design flexibility to further reduce array size and power consumption, relative to the fully connected architecture. Along with the choice of the analog and digital precoding matrices, the number of RF chains is an important design parameter in both HBF architectures, particularly in sparse channels where only a few analog beams, in the direction of dominant clusters, may be required. Furthermore, the antenna array topology will affect the beamwidth of the analog beams, and the ability to separate users channels. The authors refer the reader to [33] for a discussion of other BF techniques for mmWave channels. Of course, all BF methods are limited by the choice of SCM and relevant parameter measurements, for example, the number of clusters, C, the number of rays per cluster, L, and the angular spreads [34]. One of the key impacts of channel models on BF relates to the spatial richness in the channel. As angular spreads grow and the number of rays and clusters increases, the channel becomes richer and digital spatial multiplexing becomes far superior. In contrast, for sparser channels much of the channel behaviour can be handled effectively by analog BF, with beams pointing in a few dominant directions and users separated by digital BF with relatively few RF chains. Here, the loss of simple HBF

techniques relative to digital BF is much smaller. Hence, BF performance is inherently linked to channel properties.

D. Comparison Methodology

In this paper we consider several different metrics in order to identify key SCM parameter differences between different frequency bands and different SCMs in the same frequency band. The different metrics considered are as follows:

1) *System sum rate*:
   a) We investigate the impact of varying intra-cluster angular spread on the sum rate CDF for different frequency bands
   b) We show the impact of x-pol antenna arrays and directive APs on the sum rate CDF for a mmWave channel.
   c) The cell wide (cell edge, median and peak) sum rates are shown for different all nine environments.
   d) The impact of varying user numbers (for a fixed total number of receive antennas) is investigated on the cell wide sum rate for different environments.

2) *Channel eigenvalue properties*:
   a) We explore the impact of inter-element spacing on the average normalized eigenvalues.
   b) ULA eigenvalue distributions of different channels are shown for LOS and NLOS propagation, as well as the composite channel.

3) The impact of varying user numbers (for a fixed total number of receive antennas) is investigated on the *EDOF* for different environments.

4) We explore the impacts of varying user numbers on two different definitions of *channel connectivity*.

5) The *eigenvalue ratio* CDF is shown for randomly located and closely spaced users in order to explore the convergence to favourable propagation.

In each case, the different environment channel matrices are generated as outlined in Sec. III-B.

IV. SYSTEM SUM RATE

There are many spatial channel parameters which have an influence on the system sum rate. Due to reasons of space however, we only consider the effects of intra-cluster angular spreads. Therefore, in this section we investigate the impacts of varying the intra-cluster angular spreads, σ_ϕ and σ_θ, on the system sum rate for various simulation environments and bands. We then explore the performance of x-pol antenna elements on the resultant sum rate. Furthermore, we show the effects of channel modelling techniques on the cell edge (0.1 CDF value), median (0.5 CDF value) and peak (0.9 CDF value)[2] sum rates as well as the impacts of an increasing number of system users, whilst maintaining a fixed number of *total* RX antenna elements ($= KN$). The sum rate, R, of a multi-user MIMO system with K users, each with N antennas, can be described as[3]

$$R = B \log_2 \left| \mathbf{I}_{KN} + (\rho/M) \, \mathbf{H}\mathbf{H}^{\mathrm{H}} \right|, \qquad (8)$$

---

[2]In this paper, the authors use the notation of 0.1, 0.5 and 0.9 CDF values to refer to the 10, 50 and 90 percentiles of the CDF.

[3]The authors note that this is an upper bound for sum capacity [35].

where $\mathbf{I}_A$ denotes the $A \times A$ identity matrix, ρ is the received SNR and $\mathbf{H} = \left[\mathbf{H}_1^{\mathrm{T}}, \ldots, \mathbf{H}_K^{\mathrm{T}} \right]^{\mathrm{T}}$ denotes the composite DL channel matrix from the BS to all users.

A. The Impact of Varying Intra-Cluster Angular Spread

In Fig. 4 we plot the sum rate, R, CDF for six of the nine cellular environments[4], as a function of the antenna topology and intra-cluster azimuth and elevation angular spreads, σ_ϕ and σ_θ, respectively[5], where d_λ denotes the inter-element antenna spacing in wavelengths. Here both the AOA and AOD intra-cluster angular spreads are varied from one-quarter of their measured values, $\sigma_\phi/4, \sigma_\theta/4$, to four times their measured values, $4\sigma_\phi, 4\sigma_\theta$. In each environment, cell edge users are receiving an average SNR of -5 dB and thus the differences in the i.i.d. channel CDFs is due to the difference in p_{LOS} and PL parameters between the models. For all environments, an increase in intra-cluster azimuth and elevation angular spreads, σ_ϕ and σ_θ, produces a greater sum rate for each antenna topology resulting from less SC and, therefore, an increase in spatial diversity.

1) Antenna Topology Comparison: In nearly all environments, the ULA antenna topology has the largest sum rate over all ranges of intra-cluster angular spreads and CDF values. The ULA performs better because of its inherently larger inter-element spacings between different combinations of antennas (not adjacent antenna elements), as well as the (nearly always) wider azimuth angular spectra, compared with the (narrower) elevation angular spectra. For scenarios with a very narrow intra-cluster elevation AOD spread, such as the case in the Samimi 73 GHz environment ($\sigma_\theta^{\mathrm{AOD}} \sim \mathcal{N}(0.8, 1)$ and $\sigma_\theta^{\mathrm{AOD}} \sim \mathcal{N}(0.8, 1.3)$ degrees for LOS and NLOS, respectively), the URA essentially functions as a smaller ULA with fewer TX antenna elements, since antenna elements stacked vertically provide little additional gain[6].

2) Modelling Comparison: The Hur 28 GHz sum rate CDF has a noticeable bimodal distribution, which indicates two underlying probability density functions (PDFs), resulting from large differences in PL attenuation, β, and shadow fading variances, ϵ^2, between LOS and NLOS propagation states. Here, the LOS and NLOS shadow fading variance is $\epsilon^2 = 3.4$ dB and $\epsilon^2 = 31.8$ dB, respectively. In the other environments, such as the 3GPP 2.6 GHz environment, the two underlying PDFs are less obvious because both the PL attenuation and shadow fading variances are similar for LOS and NLOS ($\epsilon^2 = 8$ dB for LOS vs $\epsilon^2 = 12$ dB for NLOS).

3) Frequency Band Comparison: For environments in the microwave bands, there is typically both a large number of clusters, e.g., $C = 20$ clusters for 3GPP 2.6 GHz NLOS, and large inter-cluster RMS angular spreads. Therefore the performance of all antenna topologies is relatively close to the (ideal) i.i.d. scenario. Here, the impact of intra-cluster angular spreads on sum rate is minor as there is still richness

---

[4]Due to reasons of space, six cellular environments (out of the nine considered) are shown.

[5]Note that to find R per dimension, one should divide the sum rate by the number of streams [36].

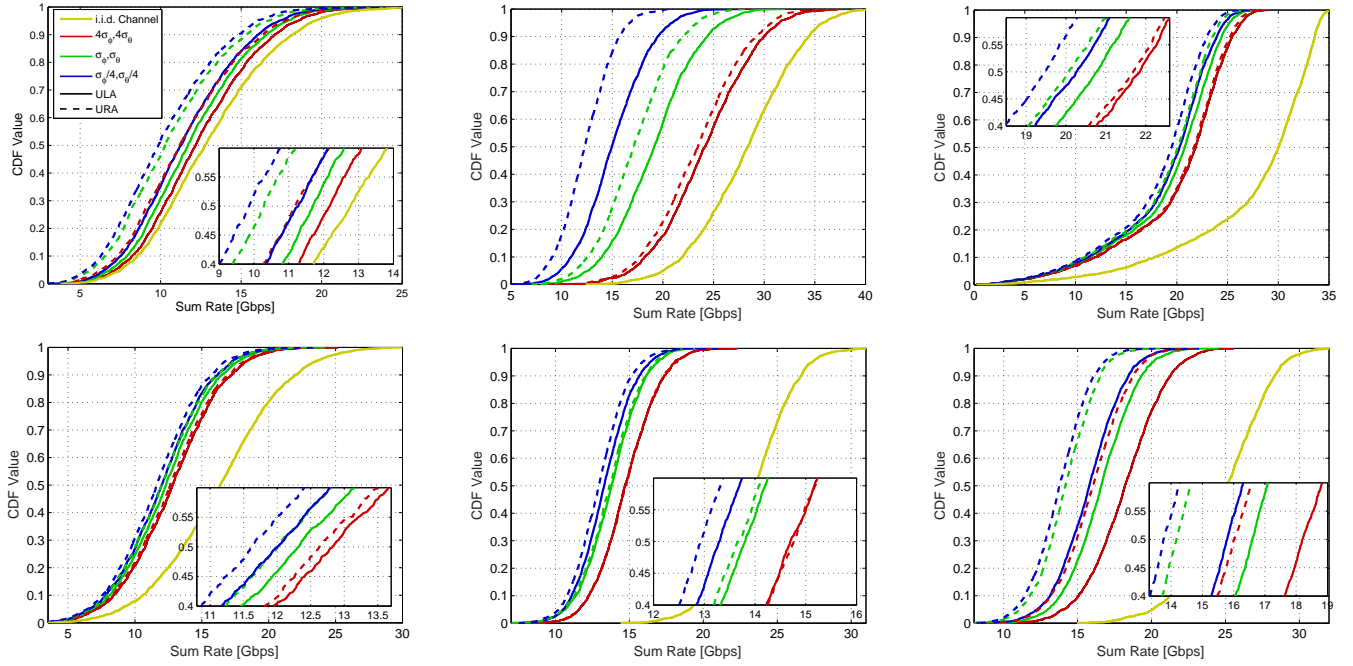[6]These heuristic remarks are supported by simulation results, not shown here for lack of space

Fig. 4: Sum rate, R, CDF as a function of antenna topology and intra-cluster azimuth and elevation angular spreads, σ_ϕ and σ_θ, for $M = 256$, $K = 8$, $N = 4$ and $d_\lambda = 1/2$. From top left to bottom right: 3GPP 2.6 GHz, Akdeniz 28 GHz, Hur 28 GHz, WPC 28 GHz, Thomas 73 GHz, Samimi 73 GHz.
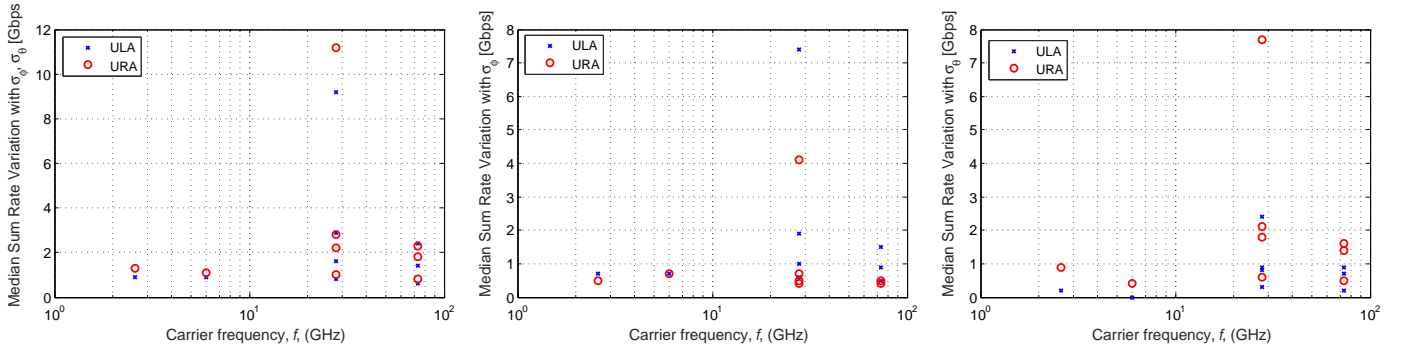

Fig. 5: Median sum rate variation vs carrier frequency, f, between four times and one quarter the tabulated intra-cluster angular spread, for the ULA and URA antenna topologies with $M = 256$, $K = 8$, $N = 4$ and $d_\lambda = 1/2$. Left: azimuth and elevation intra-cluster angular spread, σ_ϕ and σ_θ, variation. Middle: azimuth intra-cluster angular spread, σ_ϕ, variation. Right: elevation intra-cluster angular spread, σ_θ, variation.

in the scattering, even when the intra-cluster angular spread is reduced to one-quarter of its measured value. On the other hand, for mmWave bands, there are large sum rate differences between the i.i.d. CDFs and the spatially correlated cases. This can be explained by the smaller number of clusters (all mmWave environments except WPC), e.g., the Akdeniz 28 GHz channel experiences just $C = 1$ or $C = 2$ clusters 73% of the time, as well as narrow inter-cluster RMS angular spreads, particularly for NLOS users (all mmWave channels except Akdeniz 28 GHz). In the Akdeniz 28 GHz environment, the azimuth cluster central angles are uniformly distributed over the entire range of possible azimuth angles. Whereas in all other environments, azimuth cluster central angles are

distributed via a wrapped Gaussian with a mean RMS spread less than $76.5°$.

Fig. 5 summarizes the difference in median sum rate, as a function of f (for all nine environments) as the intra-cluster angular spread is varied for the ULA and URA. Here, we also show the two cases where only either the azimuth or elevation intra-cluster angular spread is varied, where the ULA and URA experience the most variation, respectively.

B. The Impact of Directive X-pol Antenna Arrays

In this section (exclusively) we investigate the impact of x-pol antenna elements, with and without directive APs, on the sum rate for the 3GPP 28 GHz channel [11]. (1) describes the

users channel with x-pol antennas and directive APs, where the vertically and horizontally polarized directive APs are

$$F^{\theta}\left(\phi_{c,l}, \theta_{c,l}\right) = \sqrt{A\left(\phi_{c,l}, \theta_{c,l}\right)} \cos\left(\zeta\right), \qquad (9)$$

$$F^{\phi}\left(\phi_{c,l}, \theta_{c,l}\right) = \sqrt{A\left(\phi_{c,l}, \theta_{c,l}\right)} \sin\left(\zeta\right), \qquad (10)$$

where ζ is the polarization slant angle [8], [11], which we assume to be $\zeta = \pm 45°$ for an x-pol antenna pair, and

$$A\left(\phi_{c,l}, \theta_{c,l}\right) = G_{\max}$$
$$- \min\left\{-\left[-\min\left[12\left(\left(\theta_{c,l} - 90\right)/65\right)^2, 30\right]\right.\right.$$
$$\left.\left. -\min\left[12\left(\left(\phi_{c,l} - 90\right)/65\right)^2, 30\right]\right], 30\right\}, \quad (11)$$

is the 3D directive AP in degrees with $G_{\max}$ denoting the maximum directive gain in dB. While x-pols are modelled at both the TX and RX antenna array, we assume that the directive AP is only modelled from the TX antenna array since users have a random orientation and should have omnidirectional RX antennas, i.e., $A(\phi_{c,l}^{\text{AOD}}, \theta_{c,l}^{\text{AOD}})$ is given in (11) and $A(\phi_{c,l}^{\text{AOA}}, \theta_{c,l}^{\text{AOA}}) = 1$.
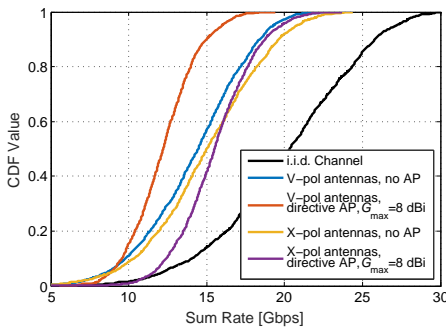
Fig. 6: Sum rate, R, CDF for 3GPP 28 GHz environment for a URA with $M = 256$, $K = 8$, $N = 4$ and $d_{\lambda} = 1/2$.

In Fig. 6 we show the effects of x-pol antennas and directive APs for a URA in the 3GPP 28 GHz channel for $M = 256$, $K = 8$ and $N = 4$. When antennas are modelled as x-pols, the 128 pairs of TX x-pols are located in 8 rows of 16 x-axis ULAs stacked vertically (relative to the z-axis). The 2 x-pols at each user are located next to each other on the x-axis. When directive APs are modelled, users are located within both the azimuth and elevation 3 dB BW, equal to $65°$ in both cases, relative to broadside of the URA. For a fair comparison between v-pol and x-pol antennas, the minimum inter-element spacing remains unchanged at $d_{\lambda} = 1/2$, and therefore the x-pol antenna array aperture is half the size of the corresponding v-pol antenna array aperture.

From Fig. 6, it can be seen that there is an increase in the sum rate when x-pol antennas are used, compared with v-pol antennas. Assuming that the SC between any two oppositely slanted antennas is negligible, the x-pol antenna array performs better since there are $M/2$ ($N/2$) fewer spatially correlated pairs of antennas at the TX (RX) antenna array. For example in the x-pol configuration, each (slanted) antenna at the user is spatially correlated with only one other (slanted) antenna,

whereas in the v-pol configuration, each antenna at the user is spatially correlated with all 3 others.

When directive APs are modelled (and users are located within the 3 dB BW), the sum rate is reduced. This is due to the reduced spatial multiplexing gain (increased SC of small-scale parameters) as well as the increased SC of users' large scale parameters, such as Rician K-factors, PL shadow fading, cluster shadowing, inter-cluster RMS angular spreads and intra-cluster angular spreads. Also, the azimuth central cluster AODs are located either $[0, \pi]$ or $[\pi, 2\pi]$ with 50% probability[7], meaning that at least 50% of the azimuth AODs are located outside the 3D BW (located between $57.5°$ and $122.5°$). As a result, a loss in sum rate is seen for scenarios with directive APs. When both x-pols and APs are modelled, however, the loss with APs is compensated by the large multiplexing gains of x-pol antennas, which are achievable in Rician fading channels [37] such as the 3GPP 28 GHz channel.
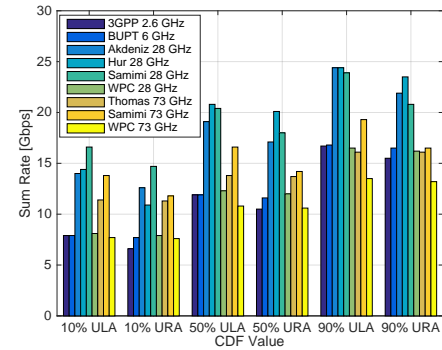
Fig. 7: Bar chart of cell edge (10%), median (50%) and peak (90%) sum rates, R, CDF values for different environments where $M = 256$, $K = 8$, $N = 4$ and $d_{\lambda} = 1/2$.
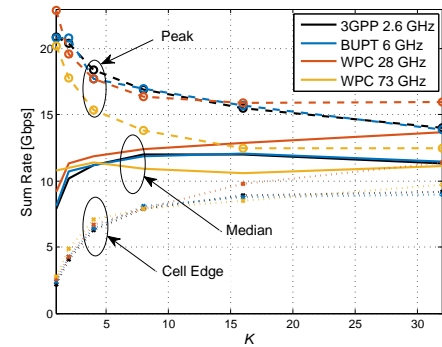
Fig. 8: Cell edge (10%), median (50%) and peak (90%) sum rates, R, CDF values as a function of the number of users, K, where $KN = 32$ is fixed and $M = 256$. All curves are for a ULA with $d_{\lambda} = 1/2$.

C. Cell Wide Sum Rate

In Fig. 7, a bar chart of the cell edge (10%), median (50%) and peak (90%) [29] sum rates is shown for a ULA and URA with $d_{\lambda} = 1/2$. The cell edge, median and peak

---

[7]The generation of central cluster angles requires assigning a positive or negative sign to all angles [8], [11]

sum rates for the different environments are directly related to the shape of the sum rate CDFs, seen in Fig. 4, which are, in turn, dependent on both the probability of LOS, p_{LOS} (shown in Fig. 3) and difference PL distributions for LOS and NLOS propagation (referring to Table I). As was seen in the sum rate CDFs, in Fig. 4, the ULA outperforms the URA. For microwave bands, where p_{LOS} is small, the CDF values are dominated by the NLOS PL distributions. Since the cell radius (link budget) is derived from the worst case (NLOS) PL values, the environments with a smaller probability of LOS propagation will have smaller CDF values, in general. For example, the 3GPP 2.6 GHz and BUPT 6 GHz microwave channels (cell radius $r = 616.2$ m) are seen to have poor cell edge sum rates.

D. Impact of User Numbers

In Fig. 8 the cell edge (10%), median (50%) and peak (90%) sum rates are shown as a function of the number of users, K, where the total number of receive antenna elements $KN = 32$ is fixed[8]. All curves are for a ULA with $d_\lambda = 1/2$ inter-element spacing. As the number of users increases from $K = 1$ (and the number of receive antennas per user decreases from $N = 32$), the cell edge and peak sum rates start to increase and decrease, respectively. The cell edge sum rates increase due to the reduced receive SC at each receiver and the resultant increase in spatial diversity by having widely separated users, and therefore antennas. However, as the number of users, K, is increased further, the cell radius shrinks due to the fixed transmit power of 15 dBm divided equally amongst the users (this is shown in Fig. 2). As a result, users become more closely spaced and experience SC amongst their parameters causing the increase in cell edge sum rate to saturate. The peak sum rate reduces as K increases since it becomes more unlikely that all K users have high individual rates.

V. Channel Eigenvalue Properties

In this section we investigate the effects of inter-element antenna spacing and propagation type on the system eigenvalue distributions of the various antenna array topologies.

A. Impact of Inter-Element Antenna Spacings

We evaluate the spatial multiplexing abilities of the antenna array topologies by considering the normalized eigenvalue magnitudes [38]. The magnitude of the ith normalized eigenvalue, $\overline{\eta}_i$, is given as

$$\overline{\eta}_i = \eta_i \Big/ \sum_{i'=1}^{KN} \eta_{i'}, \qquad (12)$$

where η_i denotes the ith eigenvalue of $\mathbf{HH}^{\text{H}}$. $\overline{\eta}_i$ is useful in constructing a measure of the maximum number of eigenchannels for spatial multiplexing.

In Fig. 9 we show the average normalized eigenvalue magnitude vs eigenvalue index as a function of antenna topology and antenna inter-element spacings for six of the nine cellular

environments. In each scenario, the average normalized eigenvalue magnitude axis is truncated at -60 dB, as all eigenvalues below this value are extremely weak and do not contribute to the spatial multiplexing capabilities of the TX antenna array. Due to the large number of TX antennas ($M = 256$), it can be seen that the i.i.d. channel curves are reasonably flat. If the number of TX antennas, M, was to increase further, one would expect the eigenvalues would converge in magnitude (known as favourable propagation [39]) to $1/16 \approx -12$ dB. For spatially correlated channels in every environment, the eigenvalue magnitudes become more equal [40] as the antenna inter-element spacing is increased from $d_\lambda = 1/8$ to $d_\lambda = 2$ wavelengths.

1) Frequency Band Comparison: For the microwave bands, the magnitude of the eigenvalues with large antenna spacings are reasonably equal and approach the i.i.d. case. For example, in the 3GPP 2.6 GHz environment, the smallest (32nd) eigenvalue for a ULA with $d_\lambda = 2$ wavelengths is only about 1 dB less than the corresponding i.i.d. eigenvalue. Whereas, in the mmWave bands, the eigenvalue magnitudes are significantly reduced. For example, in the Samimi 73 GHz environment, the mean normalized magnitude of the URA 30th eigenvalue is below -50 dB, even for large antenna inter-element spacings. This is a result of the small number of clusters and narrow angular spectra seen at mmWave frequencies which effectively reduces the multipath richness of the channel. Here, at mmWave bands, a greater inter-element spacing is required to get the same eigenvalue structure as the rich scattering microwave environments, e.g., the ULA eigenvalue structure in the Akdeniz 28 GHz for $d_\lambda = 2$ is approximately the same as the URA 3GPP 2.6 GHz at $d_\lambda = 1/2$. This is intuitive since the spatial coherence distance is inversely proportional to the angular spread. However, there are limits to this argument as a sparse mmWave channel may create a hard limit on the number of eigenvalues. Hence, any equivalence or comparison with microwave channels can be problematic.

2) Antenna Topology Comparison: As was the case for the sum rate in Sec. IV, the ULA usually performs the best in terms of spatial multiplexing over all environments, due to the inherently larger antenna spacings. The wider azimuth spectra, compared to the elevation spectra, makes it more effective for antennas to be placed in the azimuth domain. In scenarios with sparse elevation scattering, such as 3GPP 2.6 GHz, additional inter-element spacing is required for the URA to have the same eigenvalue structure as the ULA.

B. Impact of Propagation Type

In Fig. 10 we show single-user eigenvalue CDFs for six of the nine cellular environments with a ULA, $d_\lambda = 1/2$, $M = 256$ and $N = 8$. For each environment, we show the combined channel eigenvalue CDFs as well as both the LOS and NLOS eigenvalue CDFs. As the carrier frequency is increased from microwave to mmWave bands, the eigenvalue CDFs become more widely spread. For example, the Thomas 73 GHz environment only has a single eigenvalue which is much larger in magnitude than all the others. This is a result of both the lack of randomness in the channel, which is coming from narrow angular spectra and smaller numbers of

---

[8]Since we are interested in the sum rate performance when users become more closely spaced, we only consider the 3GPP 2.6 GHz, BUPT 6 GHz, WPC 28 GHz and WPC 73 GHz channel, which define SC reference distances between parameters, d_{SC}.
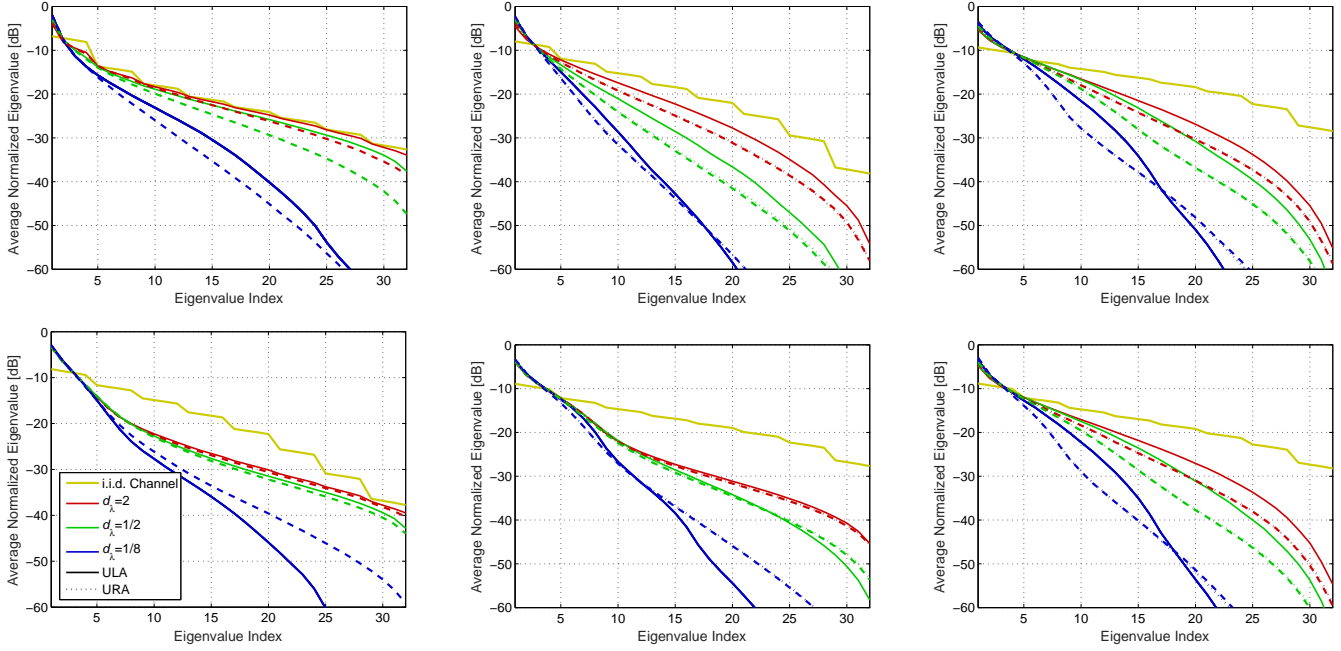
Fig. 9: Average normalized eigenvalue magnitude vs eigenvalue index as a function of antenna topology and antenna inter-element spacing, d_λ, for $M = 256$, $K = 8$ and $N = 4$. From top left to bottom right: 3GPP 2.6 GHz, Akdeniz 28 GHz, Samimi 28 GHz, WPC 28 GHz, Thomas 73 GHz, Samimi 73 GHz.

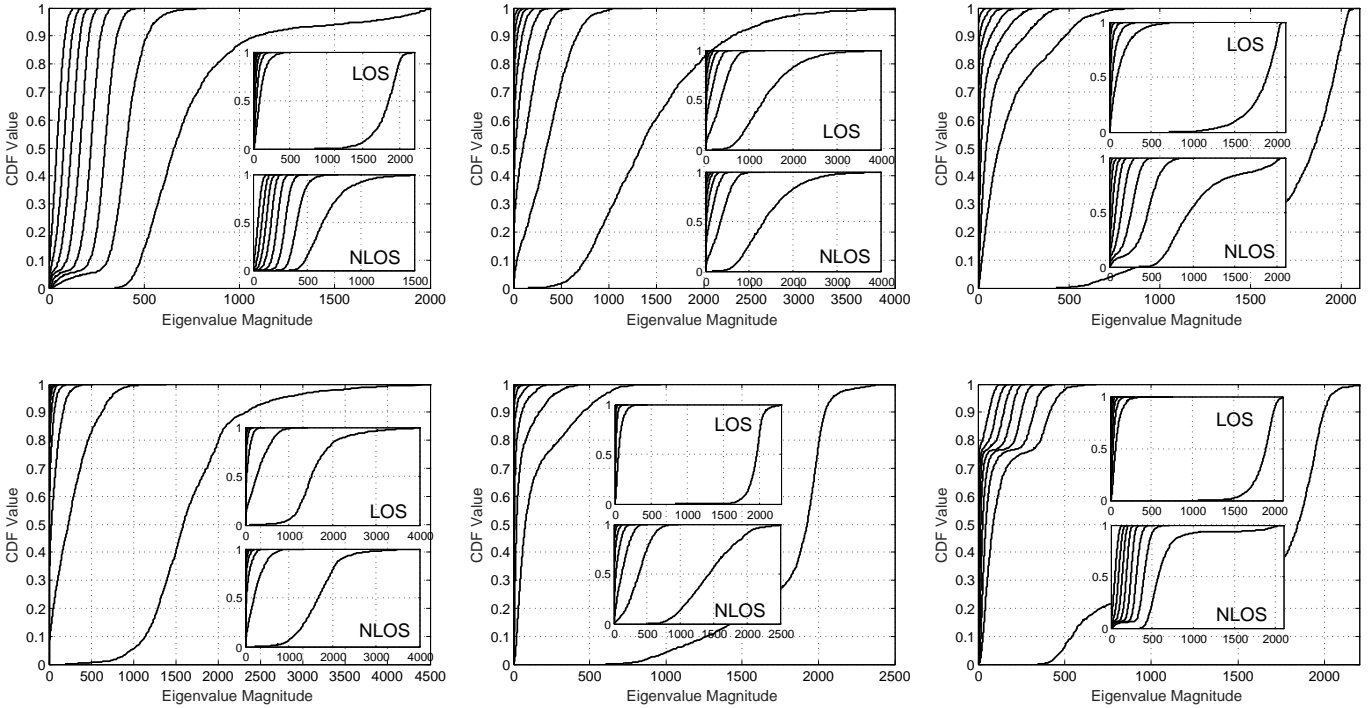
Fig. 10: Single-user ($K = 1$) eigenvalue CDFs for a ULA with $M = 256$, $N = 8$ and $d_\lambda = 1/2$. From top left to bottom right: 3GPP 2.6 GHz, Akdeniz 28 GHz, Hur 28 GHz, Samimi 28 GHz, Thomas 73 GHz, WPC 73 GHz.

clusters and subpaths. Also, the increased probability of LOS propagation is causing the combined eigenvalue CDFs to have more similarity to the LOS only case.

The distribution of the NLOS eigenvalue CDFs are completely dependent on the amount of scattering in the environments. In microwave environments, there are large numbers of clusters and subpaths, therefore the NLOS eigenvalue CDFs are more similar than the corresponding mmWave NLOS eigenvalues. On the other hand, the distribution of the LOS eigenvalue CDFs are dependent on how LOS propagation is modelled. In the simulation environments which use a Rician channel to model LOS propagation *exclusively* (i.e., all environments except Akdeniz and Samimi), the distribution of LOS eigenvalues are seen to have just one dominant CDF. The Rician K-factor mean in these environments is large (e.g., 9 dB for 3GPP 2.6 GHz) and thus the one dominant eigenvalue represents the strong specular ray. The magnitude of this dominant eigenvalue, in LOS propagation, increases as the Rician K-factor increases. Furthermore, the variance of the Rician K-factor controls the range of this dominant LOS eigenvalue. For example, the Thomas 73 GHz environment has a Rician K-factor variance of 6 dB (vs 13.68 dB for Hur 28 GHz) and the dominant LOS eigenvalue CDF is seen to be almost vertical at a magnitude around 2000 (vs a variability of almost 2000 for Hur 28 GHz). In the Samimi simulation environments, a Rician channel is used to model both LOS and NLOS propagation, therefore the LOS and NLOS eigenvalue CDFs are more similar than the environments which only use a Rician channel for LOS propagation. The small difference between LOS and NLOS eigenvalues for the Samimi environments is mostly coming from the difference in Rician K-factor mean and variance of the two propagation types. However, in the Akdeniz environments, the eigenvalues for LOS and NLOS are exactly the same[9], since the only difference in the channel modelling approach between LOS and NLOS come from different PL parameters, which do not affect the eigenvalue structure.

In summary, the largest channel eigenvalue is dependent on how the LOS channel is modelled. For Rician channels, such as 3GPP 2.6 GHz, the dominant eigenvalue represents a strong specular, deterministic, path whereas for the Akdeniz 28 GHz environment, the largest eigenvalue is coming from a lack of clusters. However, this strong difference in eigenvalue structure between the different SCMs are less obvious in the sum rate results, in Sec. IV, since p_{LOS} and variation in the PL parameters dominates the shape of the CDFs.

VI. Effective Degrees of Freedom (EDOF)

In this section we define EDOF as the number of eigenchannels which contribute to 99% of the sum rate in a multi-user system[10]. The EDOF is effectively a measure of the total number of data streams the system can simultaneously support. We explore the impact of distributing a fixed number of receiver antenna numbers into multiple users on the EDOF.

[9]This is only true for a single-users channel, as is shown in Fig. 10.

[10]Note that EDOF was previously defined in [23] for a single-input-single-output (SISO) system. We extend this definition to a multi-user scenario and set the threshold at 99% of the sum rate.
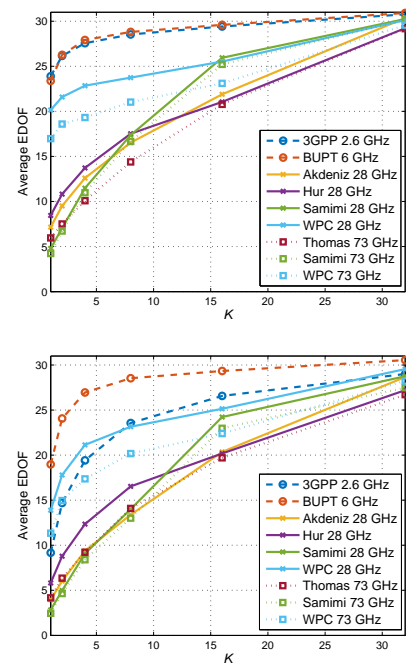

Fig. 11: EDOF as a function of the number of users, K, where $KN = 32$ is fixed, for $M = 256$ and $d_\lambda = 1/2$. Top: ULA. Bottom: URA.

In Fig. 11, we show the EDOF for the ULA and URA as a function of the users, K, where the total number of receive antennas is fixed, $KN = 32$. As the number of users, K, increases, the EDOF for each environment also increases since the SC at each user reduces, such that the channels to the 32 receive antennas are more diverse. For lower numbers of users, K, the microwave bands have more EDOF than the mmWave bands, due to the richer scattering of the microwave channel, which is reducing the SC at the receivers. However, the increase in EDOF for the microwave environments starts to saturate for larger numbers of users. On the other hand, in the limited scattering mmWave band channels, the EDOF increases dramatically as collocated antennas become distributed - and as K becomes large, the mmWave band EDOF approaches the EDOF of the microwave channel.

There is a slight decrease in the URA EDOF, relative to the ULA EDOF for all environments except 3GPP 2.6 GHz, which experiences a large drop in EDOF. This is due to their very narrow elevation spectra, in comparison to their (large) azimuth spectra. In any case where the EDOF is reduced, the number of eigenvalues which contribute to sum rate is reduced and therefore the rate per dimension [36] is increased. This results in a higher order of modulation needed. Note that the ULA EDOF at $N = 8$ (i.e., $K = 4$) can be compared to Fig. 10. For example, the ULA EDOF for the Samimi 28 GHz environment at $N = 8$ is approximately 12 for 4 users, or an average per-user EDOF of 3. Correspondingly in Fig. 10, the Samimi 28 GHz environment shows 3 eigenvalue CDFs which are contributing to 99% of the rate.

Therefore, it is more beneficial to add more users in a system rather than more antennas per user, since the increased

spatial separation of users reduces the SC at the receive end. This is more evident by considering the drop in EDOF between microwave and mmWave bands for small K and large K.

VII. Channel Connectivity

In this section, we investigate the richness of scattering and channel rank of channels from different frequency bands by considering two variations of the channel connectivity measure given in [21], [22]. Both channel connectivity measures require the computation of a *virtual* (or beamspace [41], [42]) *channel matrix* [21], [22], described for each user $k \in 1, \ldots, K$, as

$$\mathbf{V}_k = (\mathbf{A}_{\mathrm{RX}})^{-1} \mathbf{H}_k (\mathbf{A}_{\mathrm{TX}}^{\mathrm{H}})^{-1}, \qquad (13)$$

with

$$\mathbf{A}_{\mathrm{RX}} = \frac{1}{\sqrt{N}} [\tilde{\mathbf{a}}_{\mathrm{RX}}(\Theta_{\mathrm{RX},1}), \tilde{\mathbf{a}}_{\mathrm{RX}}(\Theta_{\mathrm{RX},2}), \ldots, \tilde{\mathbf{a}}_{\mathrm{RX}}(\Theta_{\mathrm{RX},N})],$$

$$\mathbf{A}_{\mathrm{TX}} = \frac{1}{\sqrt{M}} [\tilde{\mathbf{a}}_{\mathrm{TX}}(\Theta_{\mathrm{TX},1}), \tilde{\mathbf{a}}_{\mathrm{TX}}(\Theta_{\mathrm{TX},2}), \ldots, \tilde{\mathbf{a}}_{\mathrm{TX}}(\Theta_{\mathrm{TX},M})],$$

with a half-wavelength spaced ULA, as in Fig. 1,

$$\tilde{\mathbf{a}}_{\mathrm{RX}}(\Theta_{\mathrm{RX},n}) = \exp\left(j\frac{2\pi}{\lambda}\mathbf{W}_{\mathrm{RX},x}\Theta_{\mathrm{RX},n}\right), \qquad (14)$$

$$\tilde{\mathbf{a}}_{\mathrm{TX}}(\Theta_{\mathrm{TX},m}) = \exp\left(j\frac{2\pi}{\lambda}\mathbf{W}_{\mathrm{TX},x}\Theta_{\mathrm{TX},m}\right), \qquad (15)$$

and $\Theta_{\mathrm{RX},n}$ and $\Theta_{\mathrm{TX},m}$ are the nth and mth elements of $\Theta_{\mathrm{RX}} = \frac{1}{2N}[-(N-1), -(N-3), \ldots, (N-3), (N-1)]$ and $\Theta_{\mathrm{TX}} = \frac{1}{2M}[-(M-1), -(M-3), \ldots, (M-3), (M-1)]$. The two channel connectivity variations are then:

1) *Power measure*, denoted D_{power}, for a user k is then defined as the number of entries in $|\mathbf{V}_k|^2$ which contribute 90% of the total power.

2) *Rank measure*, denoted D_{rank}, for a user k is then defined as the rank of an $N \times M$ mask matrix, $\mathbf{M}$, which has entries of 1 in the corresponding locations of $|\mathbf{V}_k|^2$ which contribute to 90% of the total power, and zero elsewhere.

D_{power} measures the number of channels carrying 90% of the power but doesn't indicate the position of these channels. On the other hand, D_{rank} is a beamspace, rank based measure, somewhat similar to the EDOF without the need for an eigen-decomposition and sum rate computation.

In Fig. 12 we show the average D_{power} and D_{rank} as a function of the users, K, for a ULA, where the total number of receive antennas is fixed at $KN = 32$. As was the case for the EDOF, when the number of users, K, increases, D_{power} and D_{rank} for each environment also increases. In the case of D_{power}, the magnitude of the microwave channels keeps increasing with K, whereas for mmWave channels the magnitude saturates quickly. On the other hand, little gain in D_{rank} is seen for microwave channels beyond around $K = 10$, whereas for mmWave channels, D_{rank} increases almost linearly with the separation of receive antennas. At $K = 32$ (and $N = 1$), there becomes little difference in D_{rank} between microwave and mmWave channels.

The magnitude of D_{rank} is seen to be greatly reduced relative to D_{power}. Here, the D_{power} score is effectively measuring the number of available spatial paths, but since two paths may

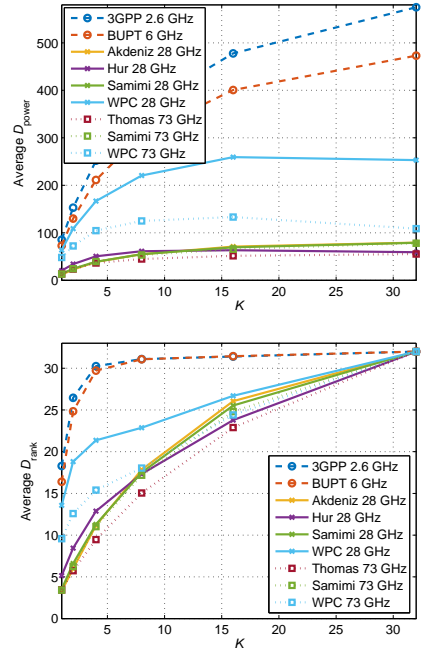Fig. 12: ULA channel connectivity as a function of the number of users, K, where $KN = 32$ is fixed, for $M = 256$ and $d_\lambda = 1/2$. Top: Average D_{power}. Bottom: Average D_{rank}.

spatially overlap, it doesn't indicate how many paths you can use effectively. For example, if number of paths between the TX and RX is equal to $MNCL$, and the TX antenna elements are perfectly correlated, the number of paths which can be used effectively is only NCL. Therefore, the D_{power} score is physically meaningful, but doesn't have the same connection to degrees of freedom as D_{rank}.

Comparing the EDOF and channel connectivity, i.e., Figs. 11 and 12, the ordering of the different channels scores are approximately the same. Both of these metrics are measuring the number of available streams and so the D_{rank} score is seen to give very similar magnitudes as the EDOF. For both, there are large differences between microwave and mmWave bands at small K, but similar values for large K.

In summary, the two channel connectivity measures, D_{power} and D_{rank}, are very different but some similarities are seen: increasing the number of users (and proportionately reducing the number of antennas per user) increases both measures. Furthermore, the D_{rank} measure gives very similar results as the EDOF since they both measure the number of *available* spatial paths for multiplexing.

VIII. Channel Convergence to Favourable Propagation

To examine the convergence to the massive MIMO regime, we now consider the eigenvalue ratio of the composite channel matrix, $\mathbf{HH}^{\mathrm{H}}$, defined as

$$\text{Eigenvalue Ratio} = \eta_{\max}/\eta_{\min}, \qquad (16)$$

where $\eta_{\max}$ and $\eta_{\min}$ are the maximum and minimum eigenvalues of $\mathbf{HH}^{\mathrm{H}}$, respectively.
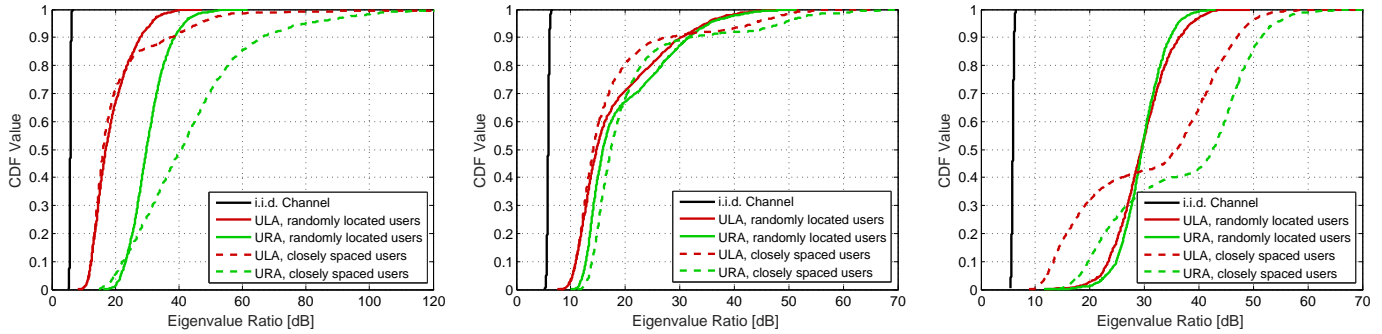
Fig. 13: Eigenvalue Ratio CDF for randomly located and closely spaced users, as a function of antenna topology for $M = 256$, $K = 8$, $N = 4$ and $d_\lambda = 1/2$. From left to right: 3GPP 2.6 GHz, BUPT 6 GHz, WPC 28 GHz.

In Fig. 13 we plot the CDF of the eigenvalue ratio as a function of different user spatial separations and antenna array topologies for 3GPP 2.6 GHz, BUPT 6 GHz and WPC 28 GHz environments, which define SC between different user parameters. For each environment we consider the two user location scenarios: users randomly located within the coverage region and users located within 2m of each other (closely spaced) on the *azimuth* plane. Closely spaced users are assumed to have common scatterers and therefore experience the same RMS angular spreads, but have independent intra-cluster angular spreads. For all environments, users being randomly located is shown to reduce the spread of the CDFs and in most cases approach the i.i.d. eigenvalue ratio. The i.i.d. channel eigenvalue ratio is close to 0 dB and almost vertical due to the large number of transmit antennas, $M = 256$, therefore approaching the massive MIMO properties of favourable propagation and channel hardening, respectively [5], [39], [43], [44]. On the other hand when users are closely spaced, there are instances where the highly correlated user channels are reducing the composite channel rank, and in turn, degrading the onset of favourable propagation.

Close user spacing is shown to have a significantly adverse impact on eigenvalue ratio convergence for all environments at high CDF values, but more so for the URA in the 3GPP 2.6 GHz environment, where the eigenvalue ratio approaches 120 dB. This is because the inter-cluster elevation AOD RMS spread becomes extremely small for large distances. For example, when all $K = 8$ users are located at a (90%) cell edge distance of 584.6 m ($r = 616.2$ m), the mean inter-cluster elevation AOD RMS spread becomes $0.5°$ and $0.9°$ for LOS and NLOS, respectively.

The CDF knee in many of the CDFs indicates a bimodal distribution and is due to the large difference in parameters between LOS and NLOS propagation. This is most noticeable and further down the CDF for the WPC 28 GHz environment, where the probability of LOS is nearly 8 times larger for users on the cell radius (referring to Fig. 3).

Comparing the relative convergence rates of the different antenna topologies in Fig. 13, it can be seen that the ULA performance is superior in all cases where users are randomly located and closely spaced, agreeing with the results presented in [45]. This is a consequence of the large aperture of the ULA, which is able to resolve more spatial variation, thus reducing SC effects. Therefore, the ULA is recommended as the antenna array approaches the onset of favourable propagation more quickly than the URA.

IX. CONCLUSION

We have shown that the system sum rate, eigenvalue structure, EDOF channel connectivity and massive MIMO convergence are significantly affected by the frequency band and antenna topology. The system performance is typically worse at mmWave bands, relative to microwave, where there is sparse scattering. However, because the channel is so sparse at mmWave bands, any change in the intra-cluster RMS angular spread drastically affects the sum rate. Furthermore, because the elevation spectra is typically narrower than the azimuth, the URA topology experiences the largest variation in sum rate with angular spread. A larger K, with a fixed KN, has been shown to both reduce the cell radius and increase the sum rate from an increase in angular diversity. However, due to the smaller cell radius, users become more closely spaced and the increase in diversity and therefore sum rate saturates.

In microwave scenarios, where the p_{LOS} is lower, the structure of eigenvalues is highly dependent on the richness of scattering. On the other hand, in mmWave bands, where the probability of LOS is higher, the structure of the eigenvalues is largely dependent on the LOS SCM. For Rician channels, the eigenvalue structure deteriorates with larger κ. However, for a PL scaled S-V LOS SCM, such as in Akdeniz et al. [12], the eigenvalues are the same as the NLOS case. The ULA is seen to have superior eigenvalue structure due to the inherently larger inter-element spacings and wider azimuth spectra, which makes it less effective for antennas to be placed vertically. These observations are seen to affect sum rate performance.

The EDOF and channel connectivity were explored for all environments as a function of the number of users with the total number of receive antennas fixed. A larger gain in EDOF and channel connectivity was seen with larger user numbers (and smaller receive antennas per user), since this provides a greater angular diversity than adding more co-located antennas. Microwave environments were shown to have larger EDOF and channel connectivity since path

numbers are larger and angular spectra wider. The two channel connectivity measures (power and rank measures) gave very different results. The power measure showed that there are a large number of paths in microwave channels, relative to mmWave channels. However, the rank measure showed a much smaller number of paths are available for effective transmission - with microwave and mmWave having the same number of paths when large numbers of single antenna users are deployed. The rank measure was also seen to have very similar results to the EDOF.

In general, the ULA topology was seen to have better performance than the URA due to the larger aperture and wide azimuth spectra in many channels. This conclusion was clearly seen in terms of the eigenvalue ratio, where the ULA was able to separate users channels more easily and thus is able to a support larger K. In mmWave channels a large number of users, each with a small number of receive antennas, is more beneficial for massive MIMO systems in terms of sum rate, EDOF and channel connectivity. This is because there are more independent scatterers per receive antenna.

REFERENCES

[1] DMC R&D Center, Samsung Electronics Co., Ltd., "5G Vision," February 2015.
[2] Z. Pi, *et al.*, "An introduction to millimeter-wave mobile broadband systems," *IEEE Commun. Mag.*, vol. 49, no. 6, pp. 101–107, June 2011.
[3] T. S. Rappaport, *et al.*, "Millimeter wave mobile communications for 5G cellular: It will work!" *IEEE Access*, vol. 1, pp. 335–349, May 2013.
[4] International Telecommunications Union (ITU) World Radiocommunication Conference (WRC), "Provisional final acts," November 2015.
[5] T. L. Marzetta, "Noncooperative cellular wireless with unlimited numbers of base station antennas," *IEEE Trans. Wireless Commun.*, vol. 9, no. 11, pp. 3590–3600, November 2010.
[6] J. G. Andrews, *et al.*, "What will 5G be?" *IEEE J. Sel. Areas Commun.*, vol. 32, no. 6, pp. 1065–1082, June 2014.
[7] T. S. Rappaport, *et al.*, "State of the art in 60 GHz integrated circuits & systems for wireless communications," *Proc. of the IEEE*, vol. 99, no. 8, pp. 1390–1436, August 2011.
[8] "3GPP TR 36.873 V12.3.0: Study on 3D channel model for LTE (release 12)," December 2016, available: http://www.3gpp.org/.
[9] A. A. M. Saleh, *et al.*, "A statistical model for indoor multipath propagation," *IEEE J. Sel. Areas Commun.*, vol. 5, no. 2, pp. 128–137, February 1987.
[10] F. R. Farrokhi, *et al.*, "Link-optimal space-time processing with multiple transmit and receive antennas," *IEEE Commun. Lett.*, vol. 5, no. 3, pp. 85–87, March 2001.
[11] "3GPP TR 38.900 V14.0.0 Technical Report: Study on channel model for frequency spectrum above 6 GHz (release 14)," June 2016, available: http://www.3gpp.org/.
[12] M. R. Akdeniz, *et al.*, "Millimeter wave channel modeling and cellular capacity evaluation," *IEEE J. Sel. Areas Commun.*, vol. 32, no. 6, pp. 1164–1179, June 2014.
[13] V. Raghavan, *et al.*, "Sublinear capacity scaling laws for sparse MIMO channels," *IEEE Trans. Inf. Theory*, vol. 57, no. 1, pp. 345–364, January 2011.
[14] O. El Ayach, *et al.*, "Spatially sparse precoding in millimeter wave MIMO systems," *IEEE Trans. Wireless Commun.*, vol. 13, no. 3, pp. 1499–1513, March 2014.
[15] M. K. Samimi, *et al.*, "3-D statistical channel model for millimeter-wave outdoor mobile broadband communications," *IEEE Intl. Conf. Commun.*, pp. 2430–2436, June 2015.
[16] Aalto University, AT&T, BUPT, CMCC, Ericsson, Huawei, INTEL, KT Corporation, Nokia, NTT DOCOMO, New York University, Qualcomm, Samsung, University of Bristol, and University of Southern California, "5G channel model for bands up to 100 GHz, white paper, V2.3," *3rd Workshop on Mobile Communications in Higher Frequency Bands, IEEE Global Commun. Conf.*, October 2016.
[17] S. Hur, *et al.*, "Proposal on millimeter-wave channel modeling for 5G cellular system," *IEEE J. Sel. Topics Signal Process.*, vol. 10, no. 3, pp. 454–469, February 2016.
[18] M. K. Samimi, *et al.*, "Local multipath model parameters for generating 5G millimeter-wave 3GPP-like channel impulse response," *IEEE Proc. European Conf. Antennas and Propag.*, April 2016.
[19] T. A. Thomas, *et al.*, "3D mmWave channel model proposal," *IEEE Veh. Technol. Conf.*, pp. 1–6, September 2014.
[20] C. T. Neil, *et al.*, "An evaluation of channel models, frequency bands and antenna topologies for 5G," *IEEE Veh. Technol. Conf.*, June 2017.
[21] K. Liu, *et al.*, "Capacity scaling and spectral efficiency in wide-band correlated MIMO channels," *IEEE Trans. Inf. Theory*, vol. 49, no. 10, pp. 2504–2526, October 2003.
[22] A. M. Sayeed, "Deconstructing multiantenna fading channels," *IEEE Trans. Signal Process.*, vol. 50, no. 10, pp. 2563–2579, November 2002.
[23] D-S. Shiu, *et al.*, "Fading correlation and its effect on the capacity of multielement antenna systems," *IEEE Trans. Commun.*, vol. 48, no. 3, pp. 502–513, March 2000.
[24] X. Gao, "Research on wideband MIMO channel measurements and modeling for IMT-Advanced system," *Ph.D. Thesis, Beijing University of Posts and Telecommunication*, 2008.
[25] M. K. Samimi, *et al.*, "Ultra-wideband statistical channel model for non line of sight millimeter-wave urban channels," *IEEE Global Commun. Conf.*, pp. 3483–3489, December 2014.
[26] G. R. MacCartney Jr., *et al.*, "Omnidirectional path loss models in New York City at 28 GHz and 73 GHz," *IEEE Proc. Intl. Symp. Personal Indoor and Mobile Radio Commun.*, pp. 227–231, September 2014.
[27] D. Tse, *et al.*, "Fundamentals of Wireless Communication," *Cambridge University Press*, 2005.
[28] J. G. Andrews, *et al.*, "Modeling and analyzing millimeter wave cellular systems," *IEEE Trans. Commun.*, vol. 65, no. 1, pp. 403–430, January 2017.
[29] J. H. Winters, "On the capacity of radio communication systems with diversity in a Rayleigh fading environment," *IEEE J. Sel. Areas Commun.*, vol. 5, no. 5, 1987.
[30] P. Kyosti, *et al.*, "WINNER II channel models, D1.1.2 V1.2," September 2007, available: http://www.ist-winner.org/deliverables/.
[31] M. Shafi, *et al.*, "5G: A tutorial overview of standards, trials, challenges, deployment, and practice," *IEEE J. Sel. Areas Commun.*, vol. 35, no. 6, pp. 1201–1221, June 2017.
[32] A. Alkhateeb, *et al.*, "Limited feedback hybrid precoding for multi-user millimeter wave systems," *IEEE Trans. Wireless Commun.*, vol. 14, no. 11, pp. 6481–6494, November 2015.
[33] R. W. Heath, Jr., *et al.*, "An overview of signal processing technqiues for millimeter wave MIMO systems," *IEEE J. Sel. Topics Signal Process.*, vol. 10, no. 3, pp. 436–453, April 2016.
[34] T. S. Rappaport, *et al.*, "Investigation and comparison of 3GPP and NYUSIM channel models for 5G wireless communications," *Available: arXiv:1707.00291v2*, July 2017.
[35] J. Lee, *et al.*, "Dirty paper coding vs. linear precoding for MIMO broadcast channels," *IEEE Asilomar Conf. on Signals, Systems and Computers*, October 2006.
[36] G. J. Foschini, *et al.*, "On limits of wireless communications in a fading environment when using multiple antennas," *Wireless Personal Commun.*, vol. 6, pp. 311–335, 1998.
[37] C. Oestges, *et al.*, "Dual-polarized wireless communications: From propagation models to system performance evaluation," *IEEE Trans. Wireless Commun.*, vol. 7, no. 10, pp. 4019–4031, October 2008.
[38] K. Haneda, *et al.*, "60 GHz spatial radio transmisson: Multiplexing or beamforming?" *IEEE Trans. Antennas and Propag.*, vol. 61, no. 11, pp. 5735–5743, November 2013.
[39] H. Q. Ngo, *et al.*, "Energy and spectral efficiency of very large multiuser MIMO systems," *IEEE Trans. Commun.*, vol. 61, no. 4, pp. 1436–1449, April 2013.
[40] C. T. Neil, *et al.*, "On the impact of antenna topologies for massive MIMO systems," *IEEE Intl. Conf. Commun.*, pp. 2030–2035, June 2015.
[41] A. M. Sayeed, *et al.*, "Beamspace MIMO for high-dimensional multiuser communication and millimeter-wave frequencies," *IEEE Global Commun. Conf.*, pp. 3679–3684, December 2013.
[42] J. Brady, *et al.*, "Beamspace MIMO for millimeter-wave communications: System architecture, modeling, analysis, and measurements," *IEEE Trans. Antennas and Propag.*, vol. 61, no. 7, pp. 3814–3827, July 2013.
[43] P. J. Smith, *et al.*, "On the convergence of massive MIMO systems," *IEEE Intl. Conf. Commun.*, pp. 5191–5196, June 2014.
[44] F. Rusek, *et al.*, "Scaling up MIMO: Opportunities and challenges with very large arrays," *IEEE Signal Process. Mag.*, vol. 30, no. 1, pp. 40–60, January 2013.
[45] X. Gao, *et al.*, "Massive MIMO performance evaluation based on measured propagation data," *IEEE Trans. Wireless Commun.*, vol. 14, no. 7, pp. 3899–3911, July 2015.

TABLE I: Environmental Spatial Parameters

Parameter	Microwave Bands			mmWave Bands						
	3GPP [8]	BUPT	WPC [16]	Hur [17]	Akdeniz [12]	Samimi [18], [26]	WPC [16]	Samimi [18], [26]	WPC [16]	Thomas [19]
f (GHz)	2.6	6	28	28	28	28	28	73	73	73
α (dB)	36.3 | 13.5	36.3 | 13.5	69.7	61.4	61.4 | 72.0	61.4	69.7	69.8	69.7	69.7
β (dB)	2.2 | 3.91	2.2 | 3.91	2 | 3	1.87 | 2.97	2 | 2.92	2.1 | 3.4	2 | 3	2.0 | 3.3	2 | 3	2.1 | 3.3
ϵ (dB)	4 | 6	4 | 6	4.1 | 6.8	1.7 | 15.9	5.8 | 8.7	3.6 | 9.7	4.1 | 6.8	5.2 | 7.6	4.1 | 6.8	4.9 | 7.6
C	12 | 20	15 | 16	12 | 20	6 | 6	X_1	X_2 | X_3	12 | 20	X_2 | X_4	12 | 20	5
L	20 | 20	7 | 7	20 | 20	10 | 10	20	X_5 | X_6	20 | 20	X_5 | X_7	20 | 20	10
κ (dB) $\sim \mathcal{N}(\mu, \sigma^2)$	$\mu=9$ | N/A, $\sigma=3.5$ | N/A	$\mu=12.4$ | N/A, $\sigma=6.6$ | N/A	$\mu=9$ | N/A, $\sigma=3.5$ | N/A	$\mu=7$ | N/A, $\sigma=6.84$ | N/A	N/A	$\mu=2.4$ | -0.4, $\sigma=2.0$ | 4.3	$\mu=9$ | N/A, $\sigma=3.5$ | N/A	$\mu=2.4$ | 1.5, $\sigma=2.0$ | 6.8	$\mu=9$ | N/A, $\sigma=3.5$ | N/A	$\mu=12$ | N/A, $\sigma=3$ | N/A
Mean ϕ^{AOA} RMS spread (°)	71.8 | 76.5	52.0 | 70.2	71.8 | 50.5	45.3 | 51.6	N/A	59.4 | 36.7	71.8 | 50.5	59.4 | 35.2	71.8 | 39.0	28.1
Mean ϕ^{AOD} RMS spread (°)	17.4 | 31.6	25.4 | 24.0	20.5 | 26.6	25.5 | 55.2	N/A	37.0 | 37.5	20.5 | 26.6	37.0 | 32.7	22.8 | 23.8	20.1
Mean θ^{AOA} RMS spread (°)	9.5 | 19.5	23.7 | 24.7	9.5 | 11.8	6.4 | 4.9	N/A	4.1 | 6.7	9.5 | 11.8	4.1 | 3.8	9.5 | 8.7	$\ln\mathcal{N}(X_8, 0.5)$
θ^{AOD} RMS spread (°)	X_9 | X_{10}	$\ln\mathcal{N}(1.1,0.4)$ | $\ln\mathcal{N}(1.2,0.8)$	X_9 | X_{10}	X_9 | X_{10}	N/A	X_9 | X_{10}	X_9 | X_{10}	X_9 | X_{10}	X_9 | X_{10}	$\ln\mathcal{N}(X_{11}, 0.6)$
ϕ_0 distribution	Gaussian	Gaussian	Gaussian	Gaussian	$\mathcal{U}[0, 2\pi)$	Gaussian	Gaussian	Gaussian	Gaussian	Gaussian
θ_0 distribution	Laplacian	Laplacian	Laplacian	Laplacian	LOS angle	Laplacian	Laplacian	Laplacian	Laplacian	Laplacian
Mean σ_ϕ^{AOA} (°)	11 | 15	24 | 29	11 | 15	2.7 | 6.8	Exp(15.5)	$\mathcal{N}(6.7, 259.2)$ | $\mathcal{N}(9.6, 404.0)$	11 | 15	$\mathcal{N}(6.7, 259.2)$ | $\mathcal{N}(5.2, 146.4)$	11 | 15	5.3
Mean σ_ϕ^{AOD} (°)	5 | 2	9 | 11	5 | 2	1.9 | 4.8	Exp(10.2)	$\mathcal{N}(1.5, 4.8)$ | $\mathcal{N}(3.0, 20.2)$	5 | 2	$\mathcal{N}(1.5, 4.8)$ | $\mathcal{N}(2.1, 47.6)$	5 | 2	6
Mean σ_θ^{AOA} (°)	7 | 7	7 | 7	$\mathcal{N}(7,5)$ | $\mathcal{N}(7,4.9)$	3.4 | 6.4	Exp(6.0)	$\mathcal{N}(1.8,4)$ | $\mathcal{N}(1.6,12.2)$	$\mathcal{N}(7,5)$ | $\mathcal{N}(7,4.9)$	$\mathcal{N}(1.8,4)$ | $\mathcal{N}(1.5,3.6)$	$\mathcal{N}(7,5)$ | $\mathcal{N}(7,4.9)$	X_{12}
Mean σ_θ^{AOD} (°)	$\frac{3}{8}Y(0.75)$ | $\frac{3}{8}Y(0.9)$	$\frac{3}{8}Y(0.75)$ | $\frac{3}{8}Y(0.9)$	$\mathcal{N}(\frac{3}{8}Y(0.75), 4.4)$ | $\mathcal{N}(\frac{3}{8}Y(0.9), 5.6)$	1.0 | 2.2	Exp(3.9)	$\mathcal{N}(0.8,1)$ | $\mathcal{N}(0.8,1)$	$\mathcal{N}(\frac{3}{8}Y(0.75), 4.4)$ | $\mathcal{N}(\frac{3}{8}Y(0.9), 5.6)$	$\mathcal{N}(0.8,1)$ | $\mathcal{N}(0.8,1.3)$	$\mathcal{N}(\frac{3}{8}Y(0.75), 4.4)$ | $\mathcal{N}(\frac{3}{8}Y(0.9), 5.6)$	X_{13}
ξ d_{SC} (m)	37 | 50	37 | 50	37 | 50	37 | 50	N/A	N/A	37 | 50	N/A	37 | 50	N/A
κ d_{SC} (m)	12 | N/A	40 | N/A	12 | N/A	12 | N/A	N/A	N/A	12 | N/A	N/A	12 | N/A	N/A
ϕ^{AOA} RMS spread d_{SC} (m)	15 | 50	44 | 8.3	15 | 50	15 | 50	N/A	N/A	15 | 50	N/A	15 | 50	N/A
ϕ^{AOD} RMS spread d_{SC} (m)	18 | 50	47 | 2	18 | 50	18 | 50	N/A	N/A	18 | 50	N/A	18 | 50	N/A
θ^{AOA} RMS spread d_{SC} (m)	15 | 50	44 | 8.3	15 | 50	15 | 50	N/A	N/A	15 | 50	N/A	15 | 50	N/A
θ^{AOD} RMS spread d_{SC} (m)	15 | 50	44 | 8.3	15 | 50	15 | 50	N/A	N/A	15 | 50	N/A	15 | 50	N/A

where $\log_{10}(Y(x)) = \max[-0.5, x - 2.1(d/1000)]$, $X_1 \sim \max[\text{Poisson}(1.8), 1]$, $X_2 \sim \mathcal{N}(5, 12.3)$, $X_3 \sim \mathcal{N}(5.3, 5.8)$, $X_4 \sim \mathcal{N}(4.6, 10.9)$, $X_5 \sim \mathcal{N}(12.4, 219.0)$, $X_6 \sim \mathcal{N}(12.8, 458.0)$, $X_7 \sim \mathcal{N}(13.2, 488.4)$, $X_8 = \max[0.3, -0.0025d]$, $X_9 \sim \ln\mathcal{N}(Y(0.75), 0.4)$, $X_{10} \sim \ln\mathcal{N}(Y(0.75), 0.4)$, $X_{11} = \max[0.4, -0.002d]$, $\log_{10}(X_{12}) = \max[0, -0.002d + 0.83]$ and $\log_{10}(X_{13}) = \max[0, -0.0023d + 0.81]$.

Callum T. Neil (S13-M17) received the B.E. (Hons.) and Ph.D. degrees in Electronic and Computer Systems Engineering from Victoria University of Wellington, Wellington, New Zealand, in 2012 and 2017, respectively. Recently, he has been researching in conjunction with Spark, New Zealand. His research interests include the modelling and analysis of wireless channel models, mmWave systems and large antenna arrays.

Pawel A. Dmochowski (S'02–M'07–SM'11) was born in Gdansk, Poland. He received a B.A.Sc (Engineering Physics) from the University of British Columbia in 1998, and M.Sc. and Ph.D. degrees from Queen's University, Kingston, Ontario in 2001 and 2006, respectively. He is currently a Senior Lecturer in the School of Engineering and Computer Science at Victoria University of Wellington, New Zealand. Prior to joining Victoria University of Wellington, he was a Natural Sciences and Engineering Research Council (NSERC) Visiting Fellow at the Communications Research Centre Canada. In 2014–2015 he was a Visiting Professor at Carleton University in Ottawa. Between 2014–2015 he was the Chair of the IEEE Vehicular Technology Society Chapters Committee. He currently serves as an Editor for IEEE Communications Letters and IEEE Wireless Communications Letters. His research interests include mmWave, Massive MIMO and Cognitive Radio systems.

Mansoor Shafi (F 93) received the B.Sc Engg degree and the Ph.D degree both in Electrical from the University of Engineering and Technology Lahore and University of Auckland respectively in 1970 and 1979. From 1975 to 1979 he was a Junior lecturer in the university of Auckland, then joined the New Zealand Post office, that later evolved to Telecom NZ and recently to Spark New Zealand. He is currently a Telecom Fellow (Wireless at Spark NZ) and an Adjunct professor at Victoria University, School of Engineering. His research interests include radio propagation, the design and performance analysis for wireless communication systems, especially antenna arrays, MIMO, cognitive radio, massive MIMO and mmWave systems. He has published over 100 papers in these areas. He is a delegate of NZ to the meetings of ITU-R and APT and has contributed to a large number of Wireless communications standards. He has co-authored two IEEE prize winning papers: (a) IEEE Communications Society, Best Tutorial Paper Award, 2004 (co shared with David Gesbert, Da-shan Shiu, Ayman Naguib and Peter Smith) for the paper, From Theory to Practice: An overview of MIMO Space time coded Wireless Systems, IEEE JSAC, April 2003, and (b) IEEE Donald G Fink Award 2011, (co shared with Andreas Molisch, Larry J Greenstein), for their paper in IEEE Proceedings April 2009, Propagation Issues for Cognitive Radio. He has also received: The IEEE Communications Society Public Service Award, 1992 For Leadership in the Development of Telecommunications in Pakistan and Other Developing Countries, and The Member of the New Zealand Order of Merit, Queens Birthday Honors 2013, For services to Wireless Communications Mansoor attends the meetings of ITU R on mobile standards as a NZ delegate. He has been co guest editor for three previous JSAC editions, IEEE Proceedings and IEEE Communications Magazine, co-chair of ICC 2005 Wireless communications and has held various editorial and TPC roles in IEEE journals and conferences.

Jianhua Zhang (SMIEE) is currently the Drafting Group (DG) Chairwoman of ITU-R IMT-2020 channel model. She received her Ph.D. degree in circuit and system from Beijing University of Posts and Telecommunication (BUPT) in 2003 and now is professor of BUPT. She has published more than 100 articles in referred journals and conferences and 40 patents. She was awarded 2008 Best Paper of Journal of Communication and Network. In 2007 and 2013, she received two national novelty awards for her contribution to the research and development of Beyond 3G TDD demo system with 100Mbps@20MHz and 1Gbps@100MHz respectively. In 2009, she received the "second prize for science novelty" from Chinese Communication Standards Association for her contributions to ITU-R 4G (ITU-R M.2135) and 3GPP Relay channel model (3GPP 36.814). From 2012 to 2014, she did the 3 dimensional (3D) channel modeling work and contributed to 3GPP 36.873 and is also the member of 3GPP "5G channel model for bands up to 100 GHz". Her current research interests include 5G, artificial intelligence, data mining, especially in massive MIMO and millimeter wave channel modeling, channel emulator, OTA test and etc.

Peter J. Smith (M93–SM01–F'15) received the B.Sc degree in Mathematics and the Ph.D degree in Statistics from the University of London, London, U.K., in 1983 and 1988, respectively. From 1983 to 1986 he was with the Telecommunications Laboratories at GEC Hirst Research Centre. From 1988 to 2001 he was a lecturer in statistics at Victoria University of Wellington, New Zealand. From 2001-2015 he worked in Electrical and Computer Engineering at the University of Canterbury. In 2015 he joined Victoria University of Wellington as Professor of Statistics. His research interests include the statistical aspects of design, modeling and analysis for communication systems, especially antenna arrays, MIMO, cognitive radio, massive MIMO and mmWave systems.